GEOLOGICA CARPATHICA, 2025, 76, 2, 71–91 https://doi.org/10.31577/GeolCarp.2025.09

Metamorphic and post-metamorphic evolution of the SE part of the Pannonian Basin in the Algyő–Ferencszállás crystalline high: Thermobarometric constraints on Variscan to Alpine events

HENRIETTA KONDOR[1,✉] and TIVADAR M. TÓTH[1]

[1]Department of Geology, University of Szeged, Szeged, Hungary

(Manuscript received March 18, 2025; accepted in revised form July 10, 2025; Associate Editor: Igor Broska)

Abstract: The metamorphic basement of the Algyő–Ferencszállás–Kiszombor area, located in the SE part of the Pannonian Basin, consists of crystalline highs covered by thick Neogene sediments. Although productive hydrocarbon reservoirs are typically found in these Neogene formations, the crystalline basement may also play a role in fluid storage and migration. However, its structure and reservoir potential remain poorly understood. This comprehensive petrological study shows that the area comprises distinct blocks with different metamorphic evolutions. The area mainly consists of gneiss varieties, genetically related through their metamorphic histories. The first regional amphibolite facies metamorphism (M1) of gneiss terrains was overprinted by a contact metamorphic (metasomatic) effect (M2) at varying crustal depths. The peak conditions of M1 in the garnet–biotite gneiss reached ~9.5–10.5 kbar and ~670–720 °C, followed by M2 overprint at T_{max}~570–630 °C. In the garnet–kyanite gneiss, M1 reached ~7.5–8.5 kbar and ~600–650 °C, with M2 at T_{max}~730 °C. In the pseudomorph-bearing gneiss, M1 peak conditions were ~6.5–7.0 kbar and ~550–580 °C, overprinted by a contact effect in the andalusite stability field. Earlier geochronological data suggest the M1 metamorphism is of Variscan age, while M2 event likely related to an Alpine, magmatic event. These gneiss terrains form neighbouring basement blocks, with proposed post-metamorphic structural boundaries. In the Ferencszállás area, a metagranite body represents an intrusion in these gneiss terrains, which may have been the source of the contact overprint. In the shallowest structural positions, low-grade greenschist facies chlorite schist (T_{max}~270–300 °C) and epidote orthogneiss occur, separated by post-tectonic structural boundaries. Considering the hydrodynamic behaviour of other buried hill reservoirs in the Pannonian Basin, the brittle structural boundaries between blocks may serve as hydrocarbon migration pathways from the adjacent over pressured sub-basins (Szeged Basin, Makó Trough) or act as fluid reservoirs.

Keywords: Pannonian Basin, Algyő–Ferencszállás–Kiszombor, metamorphic evolution, post-metamorphic structure, buried hill reservoir

Introduction

The basement of the Pannonian Basin is a complex mosaic of metamorphic blocks resulting from Mesozoic to Neogene polyphase tectonic evolution. The late stage of the basin development involved uniform subsidence of the Pannonian Basin, causing the pre-Neogene basement to be buried by thick sedimentary sequences. While most hydrocarbon (HC) reservoirs have been discovered in these formations, recent studies have highlighted the potential of fractured basement rocks as reservoirs (Schubert et al. 2007; M. Tóth 2008; Nagy et al. 2013; Molnár et al. 2015; M. Tóth & Vargáné Tóth 2020). In these basement reservoirs, fluid migration and storage are often controlled by zones of intense fracturing, including structural boundaries within the crystalline massif. These boundaries commonly separate blocks with distinct metamorphic histories. Consequently, understanding the internal structure and metamorphic evolution is crucial for both geological interpretation and HC exploration.

The metamorphic basement of the Algyő–Ferencszállás–Kiszombor (AFK) area constitutes a central part of the most significant HC system of the Pannonian Basin located in the SE part of Hungary. In this region, the basement is surrounded by Neogene basins with marls and carbonates as source rocks (Babinszki & Kovács 2018). Although the weathered upper zone of the basement is considered the primary migration pathway between source rocks and Neogene reservoirs (Babinszki & Kovács 2018), the fractured zones within the basement may also play a significant role in HC migration and storage. However, the internal structure and metamorphic evolution of the AFK basement remain poorly understood. Previous studies have documented distinct rock types in the area; however, their metamorphic histories and their spatial relationships have not been systematically investigated. While some authors interpret the AFK basement as a uniform lithostratigraphic unit (Szederkényi 1984; Lelkes-Felvári et al. 2005), others have demonstrated that it consists of segments with distinct metamorphic histories, separated by

✉ corresponding author: Henrietta Kondor
kondor.henrietta@gmail.com

post-metamorphic structural boundaries (T. Kovács & Kurucz 1984; Kondor & M. Tóth 2021). However, no comprehensive study has been carried out to map the structural build-up of the area.

The present paper aims to reconstruct the structural build-up and metamorphic evolution of the AFK basement. Core samples and thin sections from nearly 150 boreholes reaching the metamorphic basement were investigated to determine the principal rock types. Mineral chemistry analysis and thermobarometric calculations were used to determine the metamorphic evolution of these rocks. Rocks with distinct metamorphic histories were mapped, revealing their spatial relationships. The results provide a new model for the metamorphic evolution of the region and allow determination of the potential structural boundaries between rock types, highlighting potential pathways for fluid migration within the basement.

Geological setting

The Pannonian Basin, inside the Alpine–Carpathian–Dinaric orogenic belt, comprises two tectonic mega-units: ALCAPA and Tisza–Dacia (Haas 2001), which juxtaposed during large-scale Neogene strike-slip movements (Csontos et al. 1992; Fodor et al. 1999; Csontos & Vörös 2004; Fig. 1A). The basement of the Tisza–Dacia Mega-unit consists of Variscan metamorphic rocks with different metamorphic histories. Its structure was modified by large-scale tectonic deformations due to the Lower Cretaceous compressional phase (Haas 2001), resulting in a complicated nappe system throughout the pre-Neogene basement. The Tisza–Dacia Mega-unit includes four NW-facing nappes: Mecsek, Villány–Bihor, Békés–Codru and Biharia Nappe Systems (Schmid et al. 2008; Fig. 1B). During the Middle Miocene, syn-rift extension caused the development of low-angle normal faults, forming asymmetric half-graben structures and exposing metamorphic core complexes (Tari et al. 1992; Tari 1996). This event was followed by a post-rift thermal sag phase and tectonic inversion, leading to spatial shortening, the reactivation of dip-slip faults, and the uplift of metamorphic highs (Tari et al. 1999). These events resulted in general subsidence, accumulation of sediments, burial of crystalline highs, and filling of deep sub-basins (Horváth & Tari 1999).

The pre-Neogene basement of the AFK area consists of NW–SE oriented crystalline domes located at depths of ~2.5–3.0 km in the SE part of Hungary. The Szeged Basin lies to the west and the Makó Trough to the east; both separated from the domes by Miocene fault zones. The Algyő (NW) and

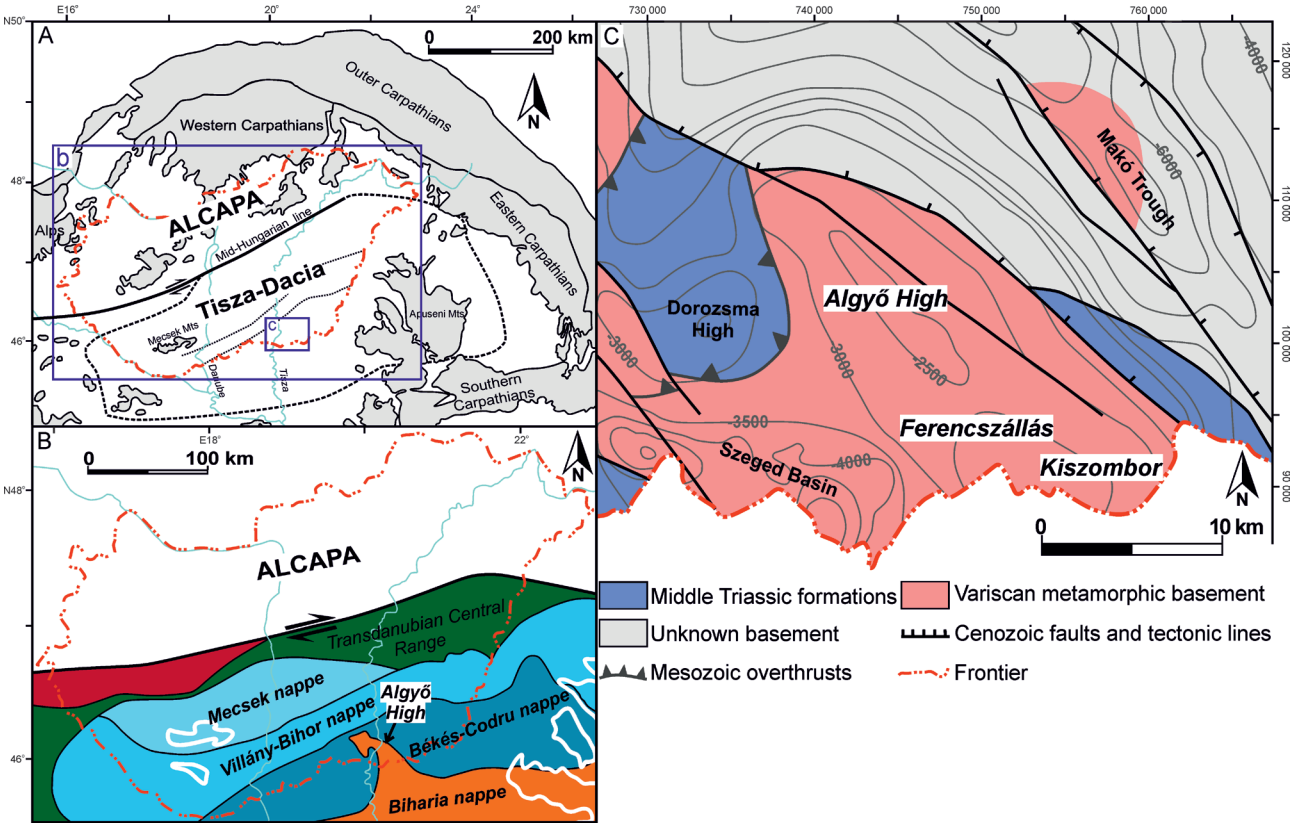

Fig. 1. A — Simplified geological map of the Carpathian–Pannonian region showing the two mega-units and the location of Hungary (modified after Csontos et al. 1992; further modified after Kondor & M. Tóth 2021). **B** — Tectonic position of the Cretaceous nappe systems within the Tisza–Dacia Mega-unit (modified after Schmid et al. 2008). **C** — Generalised pre-Cenozoic basement map of the studied area (modified after Haas et al. 2010).

Ferencszállás–Kiszombor (SE) areas form two elevated domes (Fig. 1C). According to Horváth & Árkai (2002), the two domes form the joint unit of the Algyő–Ferencszállás Metamorphic Complex. As reported by Szederkényi (1984) and Lelkes-Felvári et al. (2005), the AFK area and crystalline highs of Szeged and Dorozsma to the NW form a joint lithostratigraphic unit, referred to as the Dorozsma Complex, based on their similar geological features. While the AFK is part of the Tisza–Dacia Mega-unit, its position inside the Cretaceous nappe system is debated. According to some publications (Schmid et al. 2008; Matenco & Radivojević 2012; M. Tóth et al. 2021), it belongs to the Biharia Nappe (Fig. 1B), while others (Szederkényi 1984; Horváth & Árkai 2002) suggested it to be a part of the Békés–Codru Nappe System. Recent studies propose that the region is part of the Bihor Autochthonous Domain, exposed as a tectonic window within the Békés–Codru Nappe System (Schmid et al. 2020).

Limited information is available on the petrographic characteristics and metamorphic evolution of the area. Previous publications indicate that the metamorphic highs mainly consist of various gneisses and mica schists, occasionally intercalated by amphibolite lenses (Szalay 1977; T. Kovács & Kurucz 1984; Szederkényi 1984; Kondor & M. Tóth 2021). The granite body in the Ferencszállás area, along with the pegmatite and aplite dykes, as well as the tourmaline crystallisation within the gneissic host rocks, is prominent (Szalay 1977; T. Kovács & Kurucz 1984; Szederkényi 1984, 2007). In the Algyő High (AH), epidote orthogneiss and chlorite schist have been identified (Szalay 1977; T. Kovács & Kurucz 1984; Kondor & M. Tóth 2021). Garnet, kyanite, sillimanite, and staurolite have been documented as index minerals in gneisses and mica schist (Szalay 1977; Szederkényi 1984; Horváth & Árkai 2002; Lelkes-Felvári et al. 2003, 2005; Kondor & M. Tóth 2021). Lelkes-Felvári et al. (2003, 2005) and Szederkényi (1984) interpreted andalusite as a precursor to kyanite; however, no direct evidence supports this. Kondor & M. Tóth (2021) did not report staurolite or sillimanite in the AH area but documented kyanite aggregates forming after garnet.

According to previous studies, gneisses and mica schists underwent polyphase metamorphism (Szalay 1977; Szederkényi 1984; T. Kovács & Kurucz 1984; Horváth & Árkai 2002; Lelkes-Felvári et al. 2003, 2005; Kondor & M. Tóth 2021). By comparing the garnet zoning patterns in the NW and SE parts, Horváth & Árkai (2002) distinguished two progressive metamorphic events. The first event is characterised by the appearance of staurolite at 520–560 °C and 820–1010 MPa conditions. The maximum metamorphic conditions of the second event were 570–650 °C and 600–900 MPa in Ferencszállás, and 650–680 °C and 500–600 MPa in Algyő, indicating metamorphic overprints at different crustal depths, with slightly higher temperature and lower pressure in Algyő. In their model, kyanite, garnet, and biotite formed through the decomposition of early staurolite. Considering these results, clockwise, progressive metamorphic pathways were constructed for both sub-areas. In contrast, Lelkes-Felvári et al. (2003, 2005) suggested a high-temperature/low-pressure (HT/LP) metamorphism involving andalusite formation, followed by an amphibolite facies overprint, during which andalusite was replaced by kyanite. This model suggested a counterclockwise P–T path for the garnet–kyanite gneiss. Kondor & M. Tóth (2021) proposed that the first regional amphibolite facies metamorphism was overprinted by a contact metamorphic (metasomatic) event linked to an igneous intrusion, during which extremely fine-grained kyanite aggregates formed at the expense of garnet. As a result, the counterclockwise P–T evolution of the gneiss terrain was rejected. Based on the garnet Sm–Nd age data, Lelkes-Felvári et al. (2003) defined the first metamorphic event in the area as Permian in age (273±7 Ma). The second metamorphic event is suggested to be an eo-Alpine regional metamorphic overprint from the Late Cretaceous (82–95 Ma), based on Ar–Ar cooling ages of secondary muscovite. Balogh & Pécskay (2001) also published Ar–Ar plateaus ages of the Late Cretaceous (68.4–84.3 Ma) from the area. Horváth & Árkai (2002) agree with the second Alpine progressive metamorphic overprint but do not rule out the possibility of a polyphase Alpine evolution. Lelkes-Felvári et al. (2003) determined a Late Cretaceous–Paleocene Ar–Ar plateau age (58–70 Ma) in the AH area, interpreting it as a retrograde metamorphic overprint of the gneiss terrain.

The metamorphic evolution of epidote orthogneiss and chlorite schist in the AH area differs significantly from that of the polymetamorphic gneisses. Kondor & M. Tóth (2021) proposed an intrusive granitoid protolith for the epidote orthogneiss, with retrograde greenschist facies features. In contrast, the chlorite schist formed along a progressive greenschist facies pathway, which sometimes coincided with biotite formation.

The Cretaceous compressional event led to the formation of a nappe system in the Mesozoic sedimentary cover and the metamorphic basement of the SE part of Hungary (Szederkényi 1984; Tari et al. 1999). During this phase, nappes with different metamorphic histories were juxtaposed. This structural arrangement is evident in the adjacent Dorozsma High (DH) (Fig. 1C), where the basement is defined by, from the top to the bottom, high-grade garnet–kyanite gneiss, low-grade dolomite marble and an amphibolite-dominated domain (M. Tóth 2008; M. Tóth & Vargáné Tóth 2020). To the east of the study area, in the SW part of the Apuseni Mountains (Fig. 1A), intensely deformed dolomite marble is interpreted as a nappe boundary between the underlying Codru and the overthrusted Biharia nappes (Reiser et al. 2017a, b). Based on petrologic similarities between the garnet–kyanite gneisses in the DH and AH, Kondor & M. Tóth (2021) propose a three-part structure for the unknown deep part of the AH.

During the Late Cretaceous, the entire region was intruded by granite/granodiorite (banatite) bodies (Szalay 1977; Szederkényi 1984; Berza et al. 1998; Neubauer 2002; Reiser 2015). Szederkényi (1984) suggests that the dykes within the host gneisses, the crystallisation of tourmaline and muscovite, and the widespread enrichment of Mo, Sn, and W are all linked to the Cretaceous banatite magmatism. Kondor & M. Tóth

(2021) interpret the post-kinematic tourmaline in garnet–kyanite gneiss and the metasomatic overprint of the chlorite schist in the AH area as the result of a metasomatic hydrothermal effect from a young granite intrusion.

Syn-rift extension during the Middle Miocene resulted in numerous low-angle normal fault systems in the basement, leading to the development of metamorphic core complexes (Tari et al. 1992; Tari 1996). Matenco & Radivojevic (2012) interpreted the basement highs in the AFK area as a series of blocks linked to a WSW–ENE-oriented core complex system. They suggested that the crystalline domes of the present basement were located at different crustal depths prior to the formation of the core complex. According to geophysical interpretations (Rumpler & Horváth 1988; Posgay et al. 1996; Tari et al. 1999), the AFK is the core of a Miocene metamorphic core complex, with the tilted background block being the DH. Different metamorphic blocks of the NW, SE and central parts of the AH are likely juxtaposed along post-metamorphic normal faults, which developed during Miocene extensional events (Kondor & M. Tóth 2021). These structural elements further complicate the internal structure of the basement, where adjacent blocks may be separated by the combination of the Cretaceous thrust sheets and the Miocene low-angle normal faults.

During the post-rift thermal sag phase of the Middle Miocene, thick Neogene sediments accumulated over both the elevated metamorphic highs and the deeper basin areas (Horváth & Tari 1999). Some of these sediments later evolved into effective source rocks for hydrocarbons. The AFK area is the central part of one of the most significant local petroleum systems in the Pannonian Basin. Based on analogies (M. Tóth et al. 2007; Vass et al. 2009; Molnár et al. 2015), large-scale brittle fault zones, assumed to exist between the blocks with different metamorphic evolutions, could provide HC migration pathways or even act as reservoirs (Kondor & M. Tóth 2021).

Methods

Petrographic analyses

The crystalline basement of the AFK area was reached by a total of 144 boreholes, of which 119 boreholes provided approximately 580 thin sections for petrographic analysis. Nearly 520 thin sections from the AH area were previously investigated by Kondor & M. Tóth (2021), and the results of these analyses were utilised in this study. In the present study, approximately 60 additional thin sections from the Ferencszállás and Kiszombor areas were examined. The petrographic analyses were carried out at the Petrographic Laboratory of the Department of Mineralogy, Geochemistry and Petrology of the University of Szeged. Thin sections were analysed using an Olympus BX41 polarisation microscope. Macroscopic investigations of core samples were validated by Olympus SZX7 stereomicroscope under reflected light. Petrographic investigations provided data on mineral composition, microtextural and microstructural characteristics, and pre-, syn-, and post-kinematic mineral paragenesis. The samples were classified based on similar petrographic features, facilitating the identification of major rock types characterised by different qualitative metamorphic histories.

Analytical methods

Based on petrographic analyses, six representative thin sections, each corresponding to a main rock type (A-113, F-19, F-6, Z-7, Z-15, A-22), were selected for measurements. The chemical compositions of minerals were determined using a Hitachi TM4000Plus SEM equipped with an Oxford Instruments Xplore Compact 30 EDS detector at the Research and Core Facility Centre at the Faculty of Science, Eötvös Loránd University. The microscope was used with a 15 kV acceleration voltage, 200 pA beam current, and 30 s counting times. Measurement accuracy corresponds to the lower detection limit, which is a few tenths of a weight per cent depending on the element.

Cathodoluminescence (CL) microscopic observations were performed with a Reliotron VII CL instrument mounted on an Olympus BX43 polarisation microscope at the Petrographic Laboratory of the Department of Mineralogy, Geochemistry and Petrology of the University of Szeged. 7 kV accelerating voltage and 0.7 mA operation parameters were used during measurements.

Thermobarometry

Based on the chemical composition of minerals, calibrated thermometers and barometers, were used to estimate the pressure (P) and temperature (T) conditions of the mineral paragenesis in the rock types. The same thermobarometric methods were applied to each lithology to enable comparisons of their evolutions. For T calculation, Ti-in-biotite (Henry et al. 2005; Wu & Chen 2015), garnet–biotite (GB) (Ferry & Spear 1978; Holdaway 2000) and chlorite-based thermometers (Kranidiotis & MacLean 1987; Hillier & Velde 1991; Zang & Fyfe 1995) were utilised. P was determined using biotite–muscovite (Bt–Ms) (Wu 2020), single garnet (Wu 2019) and Si-in-phengite (Caddick & Thompson 2008) geobarometers.

Two calibration pairs were applied to jointly estimate P–T conditions. The Ti-in-biotite thermometer (Wu & Chen 2015) was coupled with a Bt–Ms barometer by Wu (2020). Additionally, Holdaway's (2000) GB thermometer was used together with the garnet barometer by Wu (2019). Various GB calibrations based on Fe–Mg exchange are available for estimating metamorphic T. The calibration of Ferry & Spear (1978) was applied, as it is more appropriate for the mineral assemblages and the T conditions characteristics of the studied rocks. In recent decades, several empirical equations have been calibrated for estimating T of low-grade metamorphic rocks, most of which consider Fe and Mg, as well as Al content in chlorite (Cathelineau & Nieva 1985; Kranidiotis &

MacLean 1987; Cathelineau 1988; Hillier & Velde 1991; Jowett 1991; Zang & Fyfe 1995; Xie et al. 1996). Among the available calibrations, the method of Hillier & Velde (1991), based on Al content, and the calibrations of Kranidiotis & McLean (1987) and Zang & Fyfe (1995), which also consider Fe and Mg, were applied.

Results

Petrographic description

Garnet–biotite gneiss

The porphyroblastic gneiss consists of biotite, white mica, quartz, and K-feldspar, with garnet porphyroblasts and occasionally significant amounts of graphite and opaque minerals. Accessory minerals include ilmenite, rutile, zircon, apatite, and titanite. A considerable amount of tourmaline occurs in most samples. Quartz-, K-feldspar-rich and white mica-, biotite-rich zones can be separated on a macroscopic scale. Typically, the gneissic structure characterises the rock. The main foliation (S2) is defined by mica flakes or quartz-rich bands. Quartz grains are generally small, sutured, occasionally sub-grained, and commonly elongated. K-feldspar crystals are usually small and rounded, though some large, slightly fractured clasts are observed. The mica-rich parts of the rock contain large amounts of graphite bands and opaque crystals along the mica bands (Fig. 2A). Garnet grains appear as large, rounded porphyroblasts or slightly elongated grains along S2. These grains often contain inclusion trails of graphite, quartz, K-feldspar, biotite, ilmenite and rutile (Fig. 2B, C). Mica flakes, bands in the matrix, and quartz inclusions within garnet occasionally intersect the S2 planes, indicating a pre-existing foliation (S1) (Fig. 2C). Ilmenite and rutile needles are also observed in the matrix with a preferred orientation. Zircon is rounded, and apatite crystals are scattered and undeformed. Titanite appears as idiomorphic and hypidiomorphic crystals,

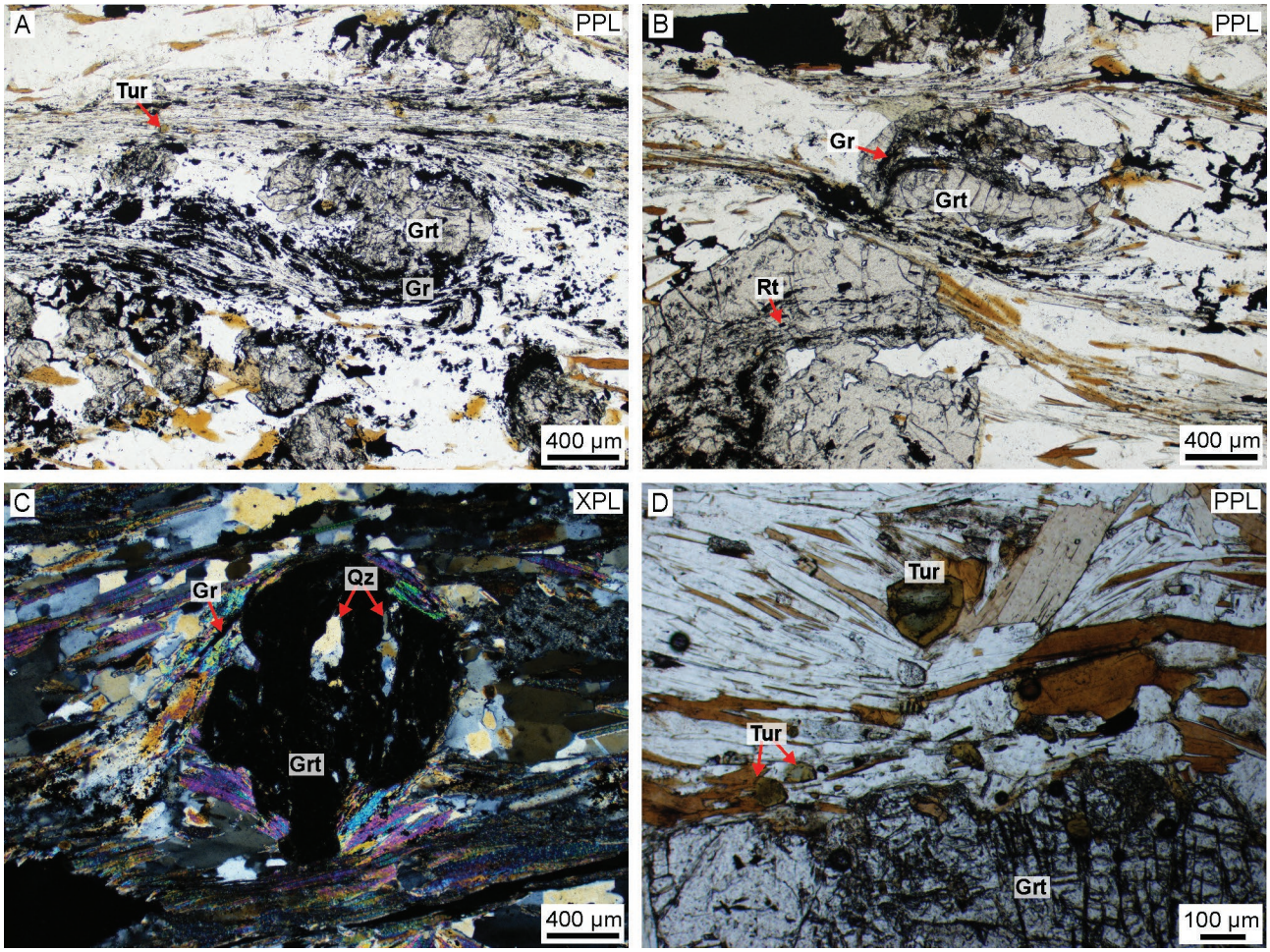

Fig. 2. Petrographic features of garnet–biotite gneiss. **A** — Garnet porphyroblast with graphite bands. **B** — Graphite and rutile inclusion trails within garnet porphyroblasts. **C** — Quartz inclusions within garnet porphyroblast aligned with the direction of the pre-existing foliation plane. **D** — Optically zoned, undeformed tourmaline crystals. PPL: plane-polarised light; XPL: crossed-polarised light. Mineral abbreviation after Whitney & Evans (2010).

some of which are slightly carbonatised. The rock commonly contains prismatic, optically zoned, undeformed, unoriented tourmaline crystals (Fig. 2D). In the deformed samples, K-feldspar clasts and quartz grains exhibit a sheared microtexture and are present as asymmetric σ-clasts. Quartz grains are elongated with undulose extinction, and deformed mica flakes, mica fishes, and S–C fabrics are also observed. Chloritisation of biotite and garnet, as well as sericitisation of K-feldspar clasts in some samples have resulted in green coloured bands and patches within the brown gneiss. Fractures are filled with limonite, sericite, and chlorite.

Garnet–kyanite gneiss

A detailed petrographic analysis of garnet–kyanite gneiss was previously provided by Kondor & M. Tóth (2021). The rock-forming minerals are quartz, K-feldspar, biotite, and white mica, with garnet porphyroblasts and fine-grained kyanite aggregates. Accessory minerals include rutile, ilmenite, titanite, monazite, zircon, and tourmaline. The main foliation (S2) is defined by bands rich in small-sized biotite, white mica, as well as quartz and K-feldspar. Larger biotite flakes (>200–400 μm) surround garnet porphyroblasts and kyanite aggregates. The garnet porphyroblasts contain inclusions of quartz, biotite, white mica, rutile, ilmenite and occasionally staurolite. Fine-grained, needle-shaped kyanite aggregates usually replace garnet or align parallel to S2 planes (Fig. 3A). In addition to large garnet porphyroblasts, small (~200–600 μm), idioblastic garnet grains with mica flakes, rutile, and ilmenite inclusions are present (Fig. 3B). Needles of ilmenite and rutile are usually oriented along the S2. Tourmaline is undeformed and unoriented. Mica fishes, K-feldspar σ-clasts, and S–C fabrics may also be observed. Chloritisation of garnet and biotite, and sericitisation of K-feldspar grains are also visible.

Pseudomorph-bearing gneiss

The rock mainly consists of white mica, quartz, biotite, and subordinately K-feldspar. It may also contain garnet porphyroblasts, albite crystals, and fine-grained kyanite and staurolite aggregates. Rutile and ilmenite are accessory phases. Most samples contain significant amounts of tourmaline. The rock exhibits a porphyroblastic, lepidoblastic texture, and a gneissic, occasionally schistose structure. The foliation is typically poorly developed and chaotic. The main foliation (S2) is defined by mica flakes, as well as quartz and K-feldspar bands. White mica primarily occurs as fine-grained crystals but may appear as large flakes in the pressure shadow zones of garnet blasts (Fig. 4A). Quartz and K-feldspar grains are usually small, sometimes elongated, and present in insignificant amounts. Larger (~400–500 μm) rounded albite clasts can also be observed within the fine-grained matrix (Fig. 4B). Garnet porphyroblasts are fractured, sheared, and wrapped by the foliation (Fig. 4A). The grains typically contain biotite and opaque inclusions. Mica flakes and garnet grains may indicate a former foliation plane (S1). Fine-grained kyanite and staurolite aggregates usually form rhombus- or cross-shaped, sometimes finger-like structures surrounded by fine-grained white mica (Fig. 4C–E). Ilmenite and rutile needles are present in significant amounts, either as inclusions in garnet, oriented in the matrix, or along kyanite–staurolite aggregates (Fig. 4C). Optically zoned, idiomorphic, hypidiomorphic and undeformed tourmaline grains are scattered throughout (Fig. 4F). Chloritisation of biotite and garnet and sericitisation of K-feldspar are typical retrograde alterations.

Chlorite schist

A detailed petrographic description of chlorite schist is provided in the previous study by Kondor & M. Tóth (2021).

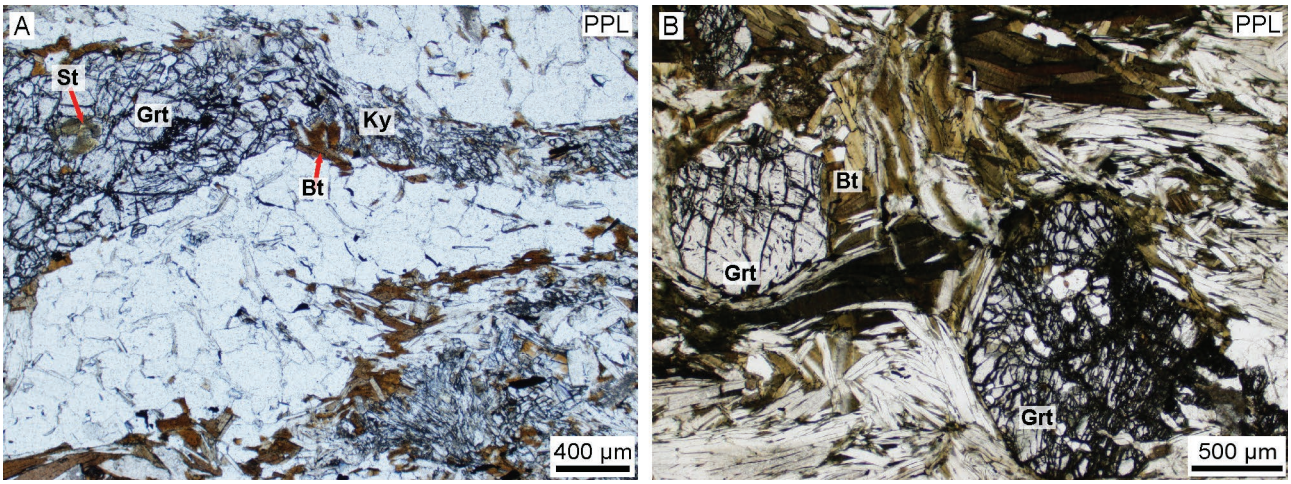

Fig. 3. Typical petrographic features of garnet–kyanite gneiss. **A** — Elongated garnet grains aligned with the S2 foliation associated with kyanite aggregates. Staurolite inclusion within garnet. **B** — Small idioblastic and large garnet grains. PPL: plane-polarised light. Mineral abbreviation after Whitney & Evans (2010).

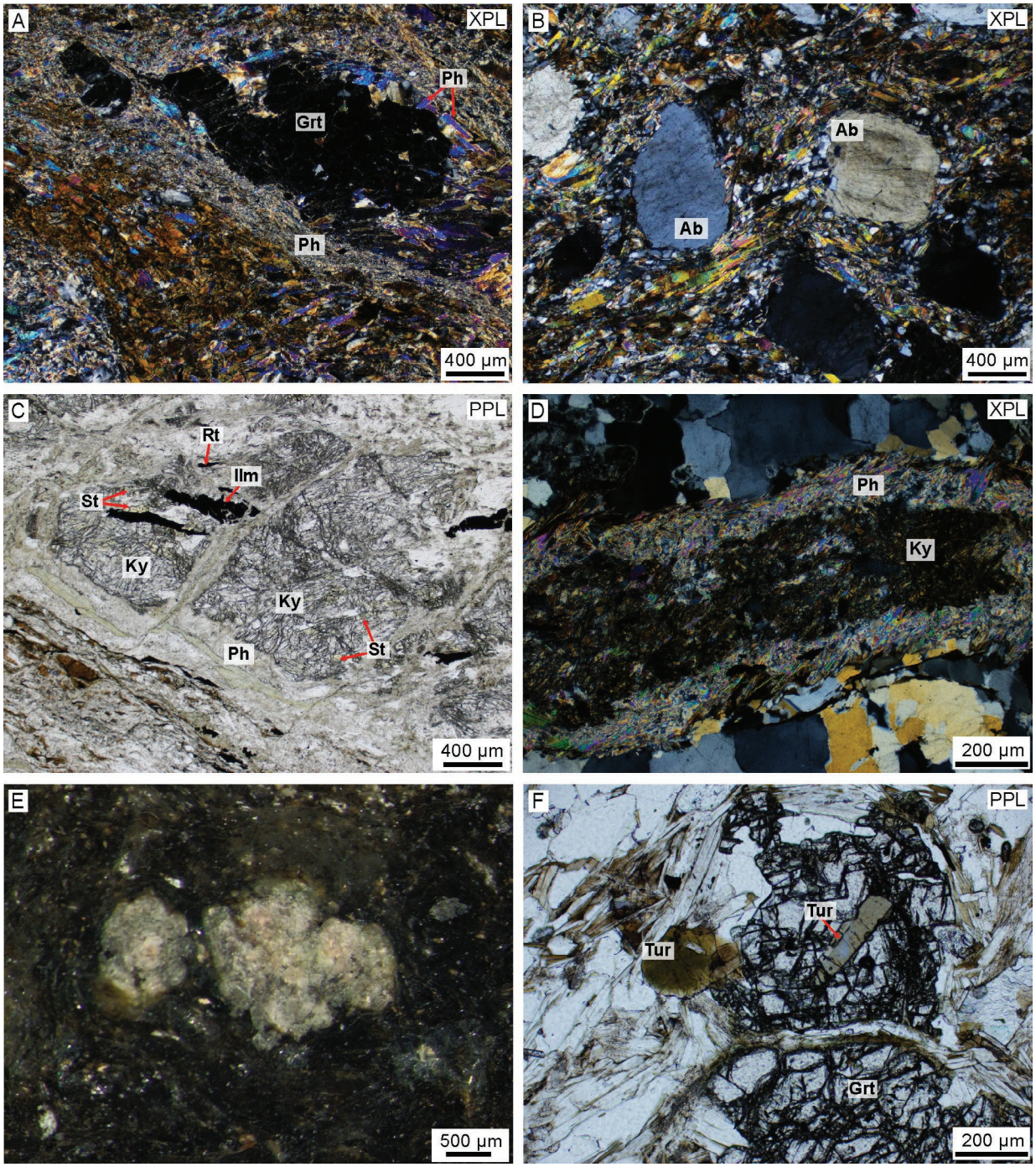

Fig. 4. Petrographic features of pseudomorph-bearing gneiss. **A** — Large white mica flakes (phengite) occurring in the pressure shadow zone of a garnet porphyroblast. Fine-grained white mica (phengite) defining the S2 foliation. **B** — Large, rounded albite clasts in the rock matrix. **C** — Fine-grained kyanite and staurolite aggregates surrounded by white mica (phengite), with oriented opaque crystals along the aggregates. **D** — Kyanite aggregates surrounded by white mica (phengite). **E** — Rhombus-shaped structure observed under a stereomicroscope. **F** — Zoned, idiomorphic tourmaline crystals. PPL: plane-polarised light; XPL: crossed-polarised light. Mineral abbreviation after Whitney & Evans (2010).

The main mineral phases of the lepidoblastic rock are chlorite, quartz, K-feldspar, and plagioclase feldspar, with occasional biotite, calcite and epidote. Accessory phases include rutile, titanite, and apatite. Chlorite plates define the foliation. Some chlorite grains are rimmed by biotite (Fig. 5A). Prismatic, idiomorphic epidote crystals and idiomorphic, hypidiomorphic opaque phases are commonly oriented along the foliation planes. The disseminated opaque grains are typically undeformed and unwrapped by foliation (Fig. 5B). Microfolding of the S1 planes has resulted in a crenulation cleavage microtexture (Fig. 5A).

Metagranite

The rock mainly consists of quartz, plagioclase feldspar, and K-feldspar, with subordinate white mica and biotite. Accessory phases include zircon, apatite, titanite, garnet, and tourmaline. The rock is weakly deformed and shows an equigranular texture. Macroscopic examination of the core samples reveals a greyish, yellowish-white rock with slight foliation (S1), defined by mica flakes, and quartz bands. Large, tabular, idiomorphic, or hypidiomorphic feldspar crystals with slightly recrystallised edges are observed. Polygonal texture (Fig. 6A), myrmekitic grains (Fig. 6B), K-feldspar twins, and perthitic texture are common. Sericitisation of K-feldspar is characteristic (Fig. 6C), with sericite forming bands along the foliation planes in the matrix. Quartz grains are often recrystallised, slightly sutured, deformed, and show undulating extinction. White mica is more dominant than biotite. Garnet grains are idiomorphic or fractured, somewhat elongated parallel to the S1. Zircon forms hypidiomorphic crystals, and hypidiomorphic tourmaline is oriented toward the S1 (Fig. 6D).

Mineral chemistry

Mineral chemistry analyses were performed on the four rock types containing metamorphic mineral paragenesis, including garnet–biotite gneiss (F-6), garnet–kyanite gneiss (A-113, F-19), pseudomorph-bearing gneiss (Z-7, Z-15), and chlorite schist (A-22). The composition of the main mineral phases, such as garnet, biotite, white mica, and chlorite was measured in various textural positions. Additionally, the composition of accessory opaque minerals and tourmaline was also analysed. Several hundred point measurements were conducted across the different mineral phases, depending on their presence and suitability for analysis.

Garnet composition

Along a core-to-rim profile of a garnet grain in the garnet–biotite gneiss, the grossular (Grs) and spessartine (Sps) components decrease, while almandine (Alm) and pyrope (Prp) increase from core to rim (Fig. 7A, B). Point measurements of other grains show similar trends. The average core composition is $Alm_{51.94–60.33}Prp_{3.79–6.98}Grs_{23.26–23.73}Sps_{9.42–20.55}$, while the rim composition is $Alm_{62.51–66.87}Prp_{7.25–11.37}Grs_{13.09–22.58}Sps_{0.28–9.89}$. The large porphyroblasts (Grt_1) in the garnet–kyanite gneiss are unsuitable for compositional profiling due to their fragmented appearance, so only individual point measurements were performed. The average core composition of Grt_1 is $Alm_{77.84–82.09}Prp_{12.22–15.68}Grs_{3.31–5.52}Sps_{1.30–2.40}$, while the rim is $Alm_{77.55–81.82}Prp_{11.33–15.07}Grs_{3.58–5.97}Sps_{0.53–3.32}$. The small idioblastic garnet grains (Grt_2) were profiled from rim to rim (Fig. 7C, D), with composition ranges from $Alm_{74.01–81.43}Prp_{12.74–19.58}Grs_{4.32–7.29}Sps_{0.00–2.92}$ in the core to $Alm_{76.80–81.07}Prp_{11.04–16.60}Grs_{3.77–6.56}Sps_{0.59–2.70}$ in the rim. Both Grt_1 and Grt_2 grains show nearly constant composition, without significant zonation. In the pseudomorph-bearing gneiss, garnet grains are intensely deformed and fractured, allowing only point measurement. The core composition is $Alm_{75.11–78.07}Prp_{8.24–13.98}Grs_{5.45–11.95}Sps_{2.22–9.73}$, while the rim is $Alm_{75.23–81.21}Prp_{9.19–13.15}Grs_{7.10–10.11}Sps_{0.76–5.47}$, displaying normal zoning with decreasing spessartine content from core to rim. Representative major oxide compositions of garnet are included in Supplementary Table S1.

Biotite composition

Analysis of biotite grains in the garnet–biotite gneiss revealed the highest Fe(II) content, calculated for 22 oxygens, in inclusions within garnet cores, ranging from 2.93 to 2.97 apfu (atom per formula unit). Lower values were observed in

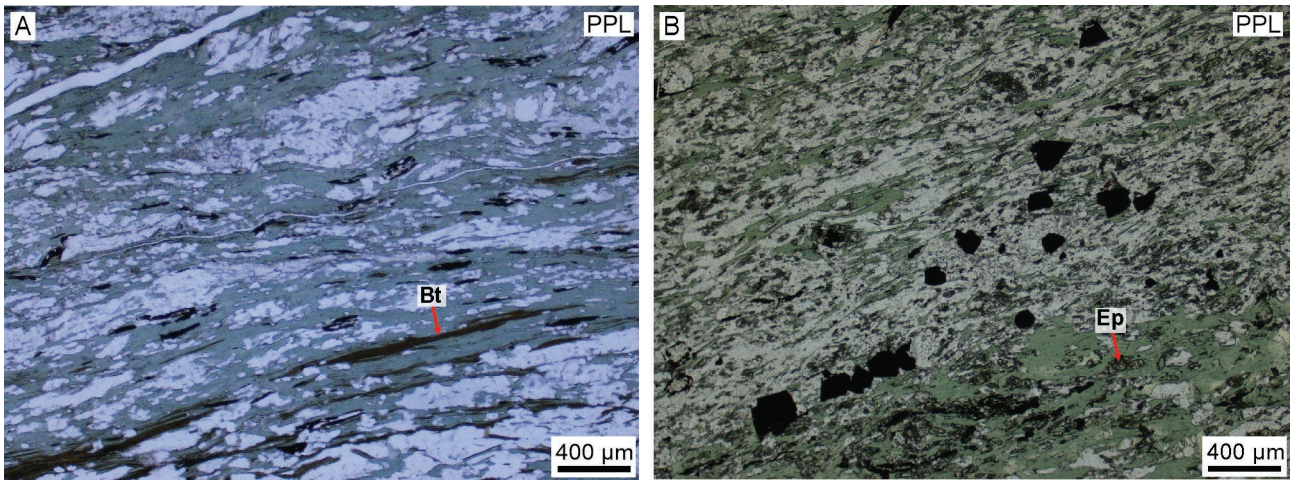

Fig. 5. Typical petrographic features of chlorite schist. **A** — Chlorite plates rimmed by biotite, with microfolding of the foliation plane. **B** — Epidote crystals and opaque grains oriented along the foliation plane. PPL: plane-polarised light. Mineral abbreviation after Whitney & Evans (2010).

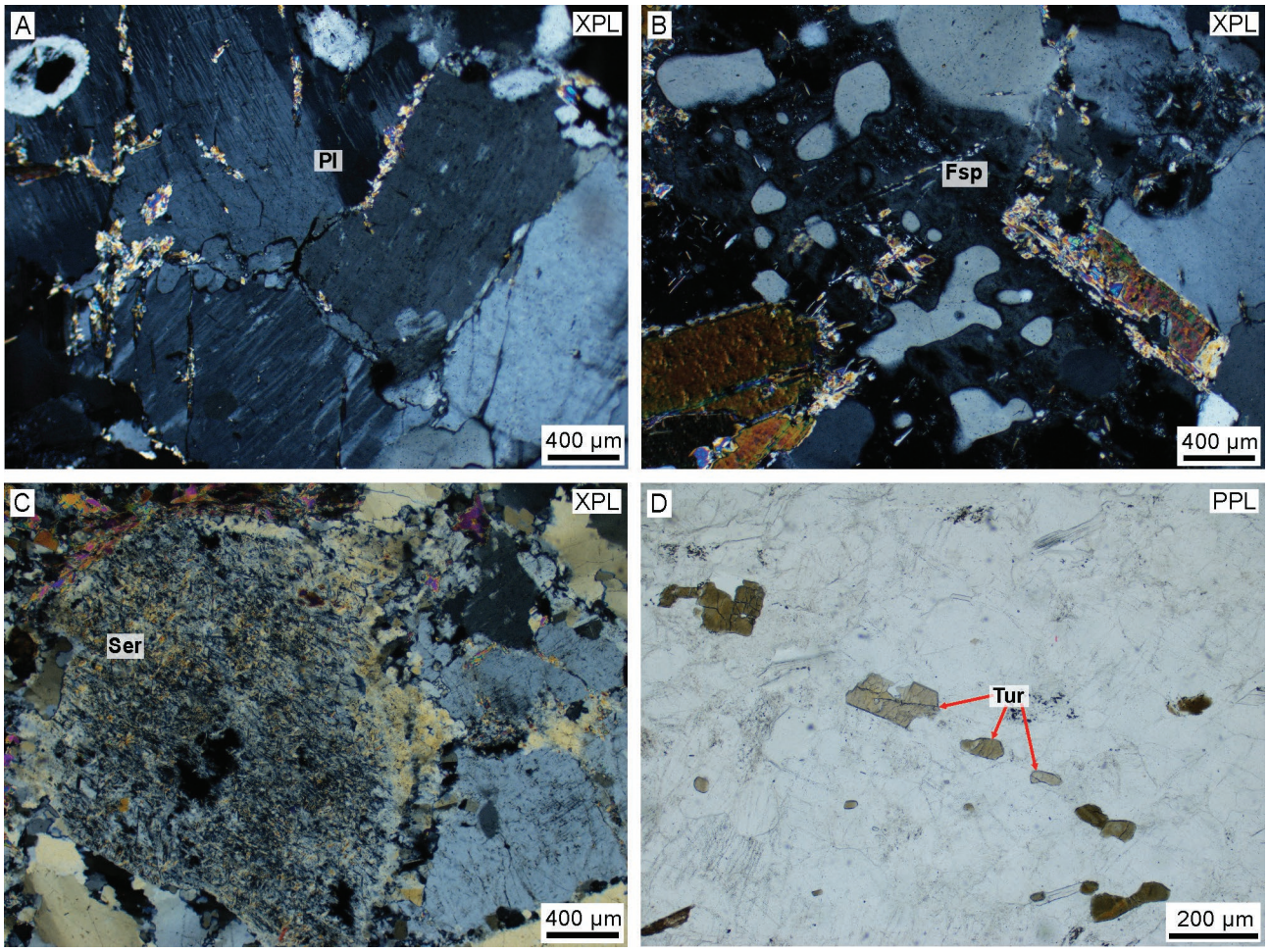

Fig. 6. Petrographic features of metagranite. **A** — Plagioclase feldspar clast displaying a polygonal microtexture. **B** —Myrmekitic grain. **C** — Sericitisation of a feldspar clast. **D** — Hypidiomorphic tourmaline oriented along the foliation. PPL: plan-polarised light; XPL: crossed-polarised light. Mineral abbreviation after Whitney & Evans (2010).

garnet rims (Fe(II)=2.55–2.66 apfu) and in the matrix (Fe(II) =2.43–2.79 apfu). In contrast, the Mg content showed an opposite trend, with values of Mg=1.83–1.90 apfu in the garnet core, Mg=2.18–2.27 apfu in the rim, and Mg=0.43–0.49 apfu in the matrix. Based on Fe/(Fe+Mg)>0.50 and Al(total)<4.0 apfu, biotite in all textural positions is classified as annite. The Ti content was similar across all textural positions. In the garnet–kyanite gneiss, biotite flakes exhibit similar compositions in all textural positions. The lowest Fe(II) content occurs in inclusions of large garnet porphyroblasts (Grt_1), ranging from 1.92 to 2.44 apfu. Larger biotite flakes in the matrix (Bt_1) are characterised by Fe(II)=2.23–2.75 apfu, while smaller biotite flakes in the matrix (Bt_2) show Fe(II)=2.07–2.65 apfu. Inclusions within the small, idioblastic garnet grains (Grt_2) have Fe(II) contents ranging from 1.94 to 2.41 apfu. Biotite inclusions in Grt_1 and Grt_2 porphyroblasts generally exhibit higher Mg content, corresponding to a phlogopite composition (Fe/(Fe+Mg)<0.50), whereas matrix flakes are classified as annite with lower Mg content. The highest Ti content was found in Bt_1 flakes (0.11–0.32 apfu) and in Grt_1 inclusions (0.18–0.33 apfu), while lower values were recorded in Bt_2 (0.06–0.24 apfu) and Grt_2 (0.12–0.21 apfu). Among the three gneiss types, biotite in pseudomorph-bearing gneiss has the highest Al(total) and Fe(II) contents, with Fe(II)=2.68–2.80 apfu in garnet inclusions and Fe(II)=2.45–3.09 apfu in the matrix. In contrast, the Ti content of biotite in this rock type was the lowest among the three gneisses. Based on the Fe/(Fe+Mg) ratio, the biotite grains are classified as annite. Representative major oxide composition of biotite is included in Supplementary Table S2.

White mica composition

White mica formulae were calculated based on 22 oxygens. In all rock types, the high Si content, low Fe+Mg content, and minimal paragonite substitution indicate a phengitic (Ph) composition. In the garnet–biotite gneiss, the white mica in the matrix exhibits Si values of 6.17–6.38 apfu and Al(total) values of 5.08–5.43 apfu. The Na content is low (0.09–0.28 apfu), while Fe+Mg ranges between 0.31–0.64 apfu. A similar

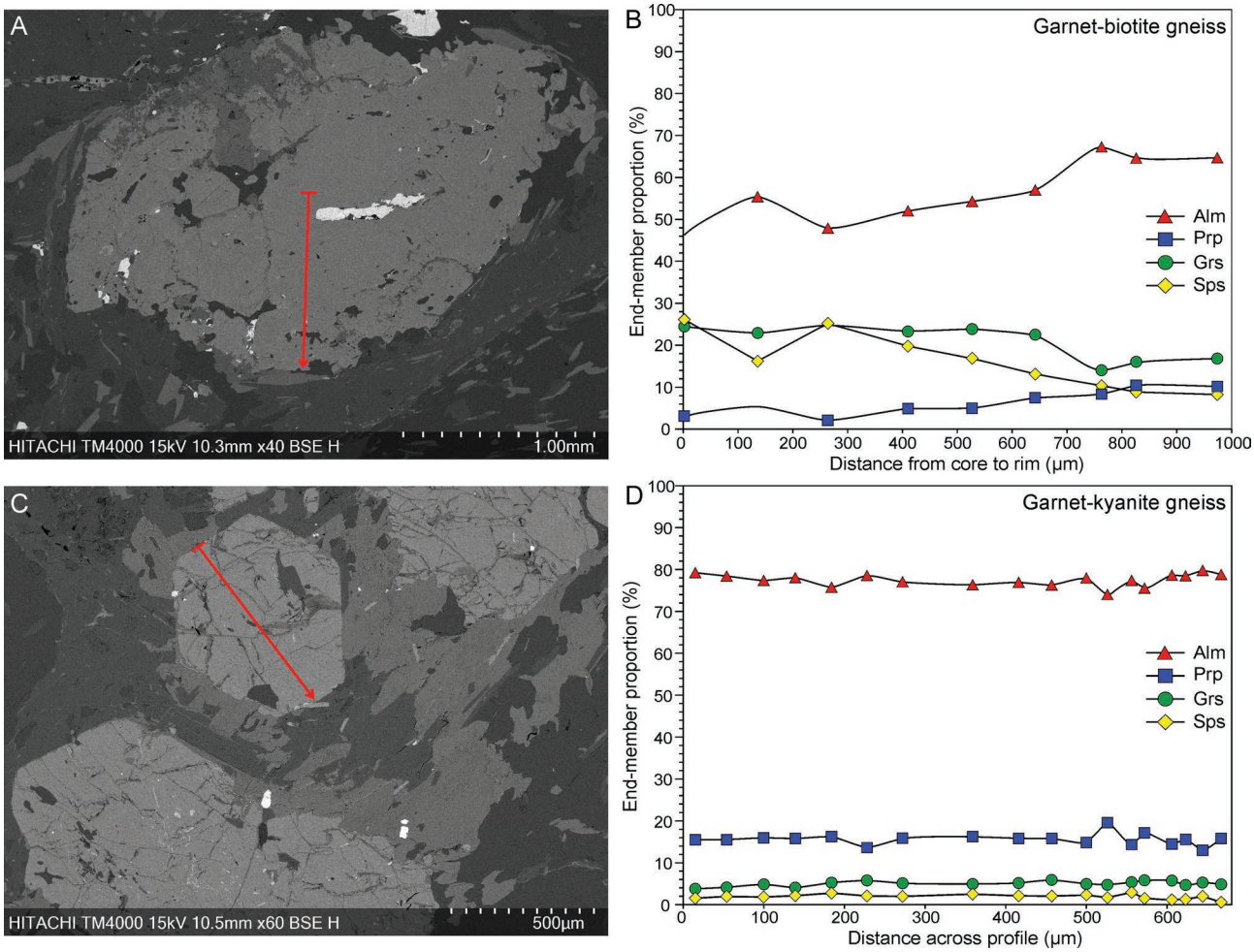

Fig. 7. Compositional profiles across garnet crystals from various lithologies. **A–B** — Core-to-rim composition profile of a garnet grain in garnet–biotite gneiss. **C–D** — Rim-to-rim composition profile of a garnet grain in garnet–kyanite gneiss. Red arrows indicate the series of measurements.

composition is observed in garnet–kyanite gneiss, where white mica appears in three textural positions (Grt_1 inclusions, matrix, and Grt_2 inclusions), all of which are identified as phengite. Si content varies between 5.98–6.34 apfu in Grt_1 inclusions, 6.02–6.24 apfu in the matrix, and 6.02–6.06 apfu in Grt_2 inclusions. Al(total) content remains consistent, ranging between 5.16–5.63 apfu in Grt_1, 5.42–5.76 apfu in the matrix, and 5.53–5.57 apfu in Grt_2. Fe+Mg values are higher in Grt_1 (0.45–0.56 apfu) and Grt_2 (0.40–0.44 apfu) compared to the matrix (0.21–0.40 apfu). The paragonite component is uniformly low (Na<0.40 apfu). In pseudomorph-bearing gneiss, the larger matrix crystals (Ph_1) have Si values of 6.07–6.26 apfu and Al(total) of 5.35–5.59 apfu, while fine-grained flakes (Ph_2) range from 5.96 to 6.11 apfu in Si and 5.51 to 5.84 apfu in Al(total). Fe+Mg contents vary between 0.23–0.42 apfu (Ph_1) and 0.19–0.57 apfu (Ph_2), with negligible paragonite substitution (Na=0.13–0.31 apfu in Ph_1 and 0.23–0.37 apfu in Ph_2). Representative major oxide composition of white mica is included in Supplementary Table S2.

Chlorite composition

Chlorite grains in the matrix of the chlorite schist shows Fe(II)=3.38–3.75 apfu, Fe(III)=0.00–0.18 apfu, and Mg=5.07–5.62 apfu content, with Mg/(Mg+Fe) ratio ranging from 0.58 to 0.61 apfu. Al^{IV} values are between 2.20–2.62 apfu, while Al^{VI} ranges from 2.49 to 2.68 apfu, with an Al(total) of 4.78–5.19 apfu. According to the chlorite formula, calculated for 28 oxygens, the rock matrix comprises clinochlorite and Fe-clinochlorite.

Opaque minerals composition

Opaque minerals in all three rock types are Fe–Ti oxides with variable FeO and TiO_2 contents. In the garnet–biotite gneiss, ilmenite (TiO_2=48.41–50.59 wt% (weight percent), FeO=39.49–40.22 wt%) and nearly pure rutile (TiO_2=92.30–95.10 wt%) occur in the matrix. The garnet–kyanite gneiss contains Fe–Ti oxides free of hematite components, including

pseudorutile (FeO=25.56–30.33 wt%, TiO_2=63.35–63.98 wt%) and ilmenite (FeO=38.26–43.39 wt%, TiO_2=40.71–49.32 wt%). In the pseudomorph-bearing gneiss, ilmenite (FeO=42.76–43.84 wt%, TiO_2=48.50–51.03 wt%) and pseudorutile (FeO=24.32 wt%, TiO_2=63.19 wt%) are present. In the chlorite schist, opaque grains (Fig. 5B) with FeO(total)=92.25–97.02 wt% were identified as magnetite. Additionally, high-Cu crystals were observed as overgrowths on idiomorphic and hypidiomorphic opaque minerals, with compositions of FeO=9.91–18.06 wt% and CuO=36.74–51.41 wt%, corresponding to bornite.

Tourmaline composition

Tourmaline crystals in the garnet–biotite gneiss exhibit distinct chemical zonation, with variations in Fe, Mg, Ca, and Na content between core and rim. Based on the Ca/(Ca+Na) ratio in the X-site and the Fe/(Fe+Mg) ratio in the Y-site, tourmaline grains belong to the alkali group with dravite composition (Fig. 8A). The core exhibits higher Fe(II) content (1.07–1.28 apfu) and lower Mg content (1.30–1.57 apfu) compared to the rim, where Fe(II)=0.71–1.29 apfu and Mg=1.47–1.85 apfu. The Ca/(Ca+Na) ratio increases from 0.06–0.17 in the core to 0.16–0.35 in the rim. In the X site, Ca increased from 0.04–0.14 apfu in the core to 0.14–0.25 apfu in the rim, whereas Na decreased from 0.67–0.81 apfu in the core to 0.42–0.69 apfu in the rim. The tourmaline crystals are Mn-free (<0.05) both in the core and on the rim. Chemical zonation is evident in the FeO/(FeO+MgO) vs MgO diagram (Pirajno & Smithies 1992), showing a continuous increase in MgO content from core to rim (Fig. 8B).

Thermobarometry

Thermobarometric calculations were conducted for P–T sensitive mineral phases in various textural positions within different rock types. For garnet–biotite gneiss, P–T calculations were made for garnet cores, garnet rims, and the matrix paragenesis. In garnet–kyanite gneiss, calculations were made for large garnet porphyroblasts and their inclusions (Grt_1), large biotite (Bt_1) and white mica flakes in the matrix ($matrix_1$), small biotite (Bt_2) and white mica grains in the matrix ($matrix_2$), as well as small garnet idioblasts and their inclusions (Grt_2). Considering the mineral chemistry, both Grt_1 and Grt_2 porphyroblasts have a nearly constant composition from the core to the rim. Thus, the distinction between core and rim measurements is irrelevant. For pseudomorph-bearing gneiss, calculations were made for garnet porphyroblasts and their inclusions (Grt), large white mica grains (Ph_1) and biotite flakes ($matrix_1$), as well as fine-grained white mica (Ph_2) ($matrix_2$) of the matrix. For chlorite schist, T was estimated from chlorite in the matrix. Since the thermobarometric data do not follow a normal statistical distribution, parametric statistics such as the mean and standard deviation are not appropriate. Therefore, the median and interquartile range (IQR) were used to characterise the P–T conditions for each textural position. The results of the thermobarometric calculation for three gneiss types are given in Table 1.

The Ti-in-biotite thermometer of Henry et al. (2005) was applied to estimate the T of all parageneses within the three gneisses, as the formation of new biotite typically characterises these assemblages. The titanium (Ti) content in biotite correlates with T, as sufficient Ti is available in the rocks to be incorporated into biotite (Forbes & Flower 1974; Robert 1976). The incorporation of Ti into biotite can be influenced by the chemical equilibrium of coexisting minerals and the presence of fluids (Henry & Guidotti 2002). Chemical equilibrium ensures a stable distribution of Ti among coexisting minerals, facilitating its incorporation into biotite. In contrast, non-equilibrium conditions can lead to variable Ti concentrations in biotite. The presence of fluid in the matrix can increase the mobility of Ti, affecting its incorporation into biotite.

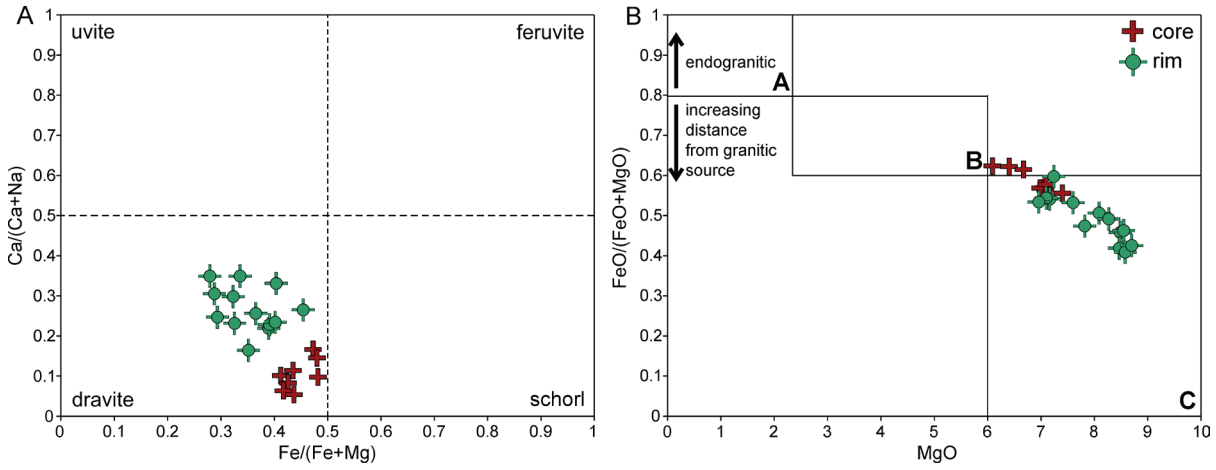

Fig. 8. Tourmaline classification diagrams. **A** — Tourmaline classification based on Ca/(Ca+Na) in the X-site and Fe/(Fe+Mg) in the Y-site. **B** — FeO/(MgO+FeO) vs. MgO diagram of the analysed tourmaline crystals, illustrating the relationship between composition and formation environment. A: tourmalines associated with endogranitic to proximal environments. B: tourmalines from proximal to distal environments. C: tourmalines from distal environments and fluid-precipitated tourmalines (modified after Pirajno & Smithies 1992).

Table 1: Results of the thermobarometric calculations. The values are characterised by the robust median and interquartile range (IQR).

Rock type	Texture position	Henry et al. (2005)	Wu (2020)		Wu (2019)		Ferry & Spear (1978)	Caddick & Thompson (2008)
		Ti-in-Bt (°C)	Ti-in-Bt (°C)	Bt–Ms (kbar)	GB (°C)	Grt (kbar)	GB (°C)	Si-in phengite (kbar)
Garnet–biotite gneiss	Grt core	558±33	–	–	728±31	11.5±1.3	688±12	–
	Grt rim	603±3	–	–	626±36	9.9±0.5	582±39	–
	matrix	588±24	–	–	625±29	10.0±0.7	591±44	8.3±0.7
Garnet–kyanite gneiss	Grt_1	640±10	594±43	7.5±1.3	–	–	545±46	6.7±0.4
	$matrix_1$	655±25	633±24	8.0±0.9	–	–	605±34	–
	$matrix_2$	600±40	572±72	6.1±1.4	–	–	582±22	6.2±1.1
	Grt_2	610±38	478±37	5.0±0.7	–	–	596±42	4.6±0.8
Pseudomorph-bearing gneiss	Grt	558±3	–	–	579±5	6.7±0.1	553±3	–
	$matrix_1$	545±8	472±87	4.1±1.5	564±26	4.9±0.6	531±41	5.2±1.4
	$matrix_2$	–	548±13	5.4±0.2	–	–	–	5.1±1.2

These factors contribute to the uncertainty of the T estimates derived from this method. T calculation based on the Ti and Mg/(Mg+Fe) relationship (Fig. 9) yielded values of 558 ±33 °C in the garnet core, 603±3 °C on the garnet rim of the garnet–biotite gneiss, and 588±24 °C in the biotite flakes of the matrix. A T of 640±10 °C was estimated for inclusions in Grt_1 blasts within garnet–kyanite gneiss. The peak T of 655 ±25 °C was calculated for Bt_1 ($matrix_1$). For Bt_2 ($matrix_2$), a T of 600±40 °C was obtained, while inclusions in Grt_2 blasts yielded a T of 610±38 °C. 558±3 °C was determined for biotite inclusions in garnet grains of pseudomorph-bearing gneiss, and 545±8 °C for matrix biotite flakes ($matrix_1$).

The Ti-in-biotite thermometer of Wu & Chen (2015) was coupled with a Bt–Ms geobarometer by Wu (2020). This method applies to metapelites containing an Al_2SiO_5 phase, making it unsuitable for estimating P–T conditions of garnet–biotite gneiss. The technique can be used for the garnet–kyanite gneiss and pseudomorph-bearing gneiss. P–T values of 594±43 °C and 7.5±1.3 kbar were calculated for Grt_1 in garnet–kyanite gneiss, while 633±24 °C and 8.0±0.9 kbar were determined for $matrix_1$. For $matrix_2$, P–T conditions of 572±72 °C and 6.1±1.4 kbar were obtained. For Grt_2, values of 478±37 °C and 5.0±0.7 kbar were calculated. The calibration could not be applied to garnet grains in pseudomorph-bearing gneiss due to the absence of white mica inclusions. For $matrix_1$, the method determined 472±87 °C and 4.1 ±1.5 kbar. P–T calculation for $matrix_2$ is uncertain because fine-grained white mica is not associated with the formation of T-sensitive new biotite. For $matrix_2$, the method yielded 548±13 °C and 5.4±0.2 kbar. However, the applied Bt–Ms geobarometry is subject to some uncertainty, as the composition of the white micas measured in these rocks mostly corresponds to phengitic compositions.

The garnet barometer (Wu 2019) combined with the GB thermometer of Holdaway (2000) applies to metapelites without Al_2SiO_5 phase or plagioclase feldspar. The approach is based on the Fe^{2+}–Ca^{2+} net transfer reaction between coexisting garnet, titanite, ilmenite, and quartz, where Ca incorporation into garnet positively correlates with P. Considering the mineral chemistry, garnet grains in the garnet–kyanite gneiss have a very low Ca content. In rocks with low Ca content, the Ca concentration in garnet is independent of P and is determined solely by the available Ca. For such compositions, calculated P values are likely underestimated and are minimal P values. Therefore, the method does not apply to garnet–kyanite gneiss but is suitable for garnet–biotite gneiss and pseudomorph-bearing gneiss with a higher Ca content. Using this method, P–T conditions of 728±31 °C and 11.5±1.3 kbar were determined for the garnet core and 626 ±36 °C and 9.9±0.5 kbar for the garnet rim in garnet–biotite gneiss. For the garnet rim and matrix biotite flakes (matrix), 625±29 °C and 10.0±0.7 kbar were determined. In pseudomorph-bearing gneiss, P–T conditions of

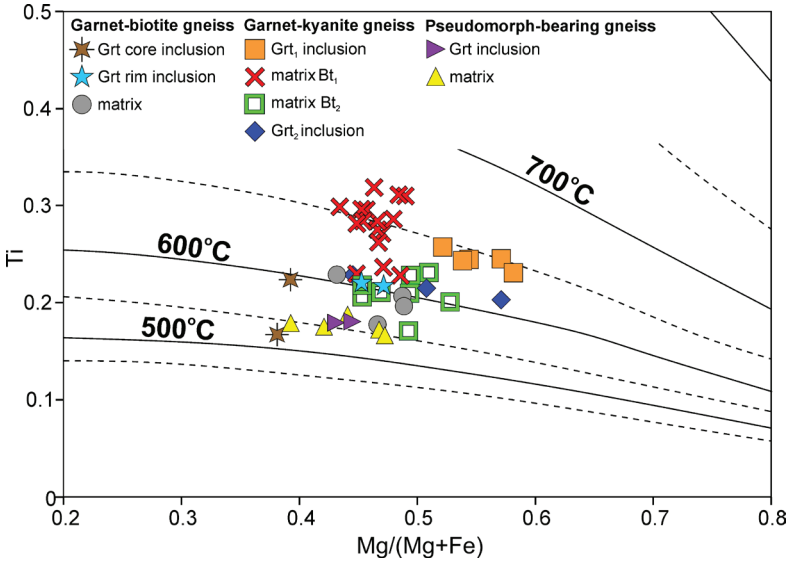

Fig. 9. Ti-in-biotite thermometer (Henry et al. 2005). Symbols in the diagram represent the Ti vs. Mg/(Mg+Fe) of biotite from various lithologies.

579±5 °C and 6.7±0.1 kbar were estimated for garnet blasts, and 564±26 °C and 4.9±0.6 kbar for matrix biotite ($matrix_1$).

Reference P ranges for the GB thermometer of Ferry & Spear (1978) were taken from the garnet geobarometer (Wu 2019) for garnet–biotite gneiss and pseudomorph-bearing gneiss, and from the Bt–Ms geobarometer (Wu 2020) for garnet–kyanite gneiss. The T estimated for the garnet core in garnet–biotite gneiss at ~10–13 kbar is 688±12 °C, while for the garnet rim at ~9–10 kbar is 582±39 °C. The T for the matrix is calculated to be 591±44 °C at ~9–11 kbar. For Grt_1 and their biotite inclusions in garnet–kyanite gneiss, 545±46 °C was determined at ~6–9 kbar. The rims of Grt_1 porphyroblasts and associated matrix Bt_1 ($matrix_1$) show T of 605±34 °C at ~7–9 kbar. Grt_2 idioblasts have a T of 596±42 °C within a P range of ~ 4–6 kbar. The rims of Grt_2 porphyroblasts and matrix Bt_2 ($matrix_2$) have a T of 582±22 °C at ~5–7 kbar. The conditions for the garnet porphyroblasts in pseudomorph-bearing gneiss were determined to be 553±3 °C at ~6–7 kbar. The conditions for garnet rim and matrix biotite ($matrix_1$) were calculated to be 531±41 °C at ~4–5 kbar.

Si-in-phengite barometers were also used to estimate P conditions, as the composition of the white micas measured in gneisses corresponds to phengitic compositions. Over the last few decades, several phengite-based geobarometer calibrations have been developed based on the relationship between P and Si content in phengite (Massonne & Schreyer 1987; Caddick & Thompson 2008; Kamzolkin et al. 2016). The method is typically applied to high-P metamorphic rocks, such as eclogites, where phengite is a typical phase. Massonne & Schreyer's (1987) geobarometer is exclusively based on the Si content of phengite, neglecting Mg content, which correlates positively with both Si content and P through Tschermak substitution, resulting in a minimum P value in the studied gneisses. The barometer of Kamzolkin et al. (2016), which considers Al, Mg, Fe, and Si in phengite, tends to overestimate P conditions for gneisses due to the T-dependent nature of Fe. The method of Caddick & Thompson (2008) was calibrated for low- to medium-grade metapelites, considering both P-dependent Si and Mg. This method is suitable for all three gneisses. For phengite flakes in the matrix of garnet–biotite gneiss, 8.3±0.7 kbar was estimated. In garnet–kyanite gneiss, P was determined as 6.7±0.4 kbar for inclusions of Grt_1, 6.2±1.1 kbar for matrix ($matrix_2$), and 4.6±0.8 kbar for phengite inclusions of Grt_2. In pseudomorph-bearing gneiss, 5.2±1.4 kbar was determined for Ph_1 flakes ($matrix_1$), while Ph_2 flakes ($matrix_2$) resulted in 5.1±1.2 kbar.

The thermometers used for chlorite schist are based on the Al^{IV} content in chlorite crystals, which correlates with T. Using the formula $T=249.56Al^{IV}-320.28$ of Hillier & Velde (1991), a T of 293±29 °C was determined. Further observations revealed that, besides Al, the Fe and Mg content in the crystals is also T-dependent and influenced by the geological environment. Using the formula $T=106(Al^{IV}+0.7[Fe/(Fe+Mg)]+18$ proposed by Kranidiotis & MacLean (1987), a T of 308±10 °C was determined. Applying the formula $T=106.2(Al^{IV}-0.88([Fe/(Fe+Mg)]-0.34))+17.5$ from Zang & Fyfe (1995) a T of 274±15 °C was calculated.

Discussion

Metamorphic evolution

Garnet–biotite gneiss

Microtextural characteristics of the rock suggest a monometamorphic origin with a retrograde overprint. The metamorphic paragenesis is represented by quartz, K-feldspar, biotite, garnet, rutile, and locally graphite. Two foliation planes can be identified: the main S2, and a pre-existing S1 foliation resulting from two distinct deformation phases. Inclusion trails in garnet blasts (Fig. 2B,C) suggest the pre-kinematic growth of garnet relative to the S2 foliation. The chemical zoning profile of the garnet blasts, characterised by decreasing grossular and increasing pyrope content towards the rim (Fig. 7A,B), indicates grain growth under conditions of decreasing P and increasing T. This trend aligns with Ti-in-biotite thermometry results. However, the lower T values compared to the GB methods in the core reflect non-equilibrium conditions during garnet growth. Based on GB thermometers and garnet barometry, peak metamorphic conditions in the garnet core were estimated to be P_{max}~11.0–12.0 kbar and T_{max} ~670–720 °C. Conditions of ~9.5–10.5 kbar and ~570–630 °C were estimated for the garnet rim and the coexisting matrix biotite. For the phengite flakes of the matrix, P values of ~8.0–8.5 kbar can be estimated, suggesting that the phengite formed along a retrograde path due to decompression. These results indicate that the garnet–biotite gneiss underwent a progressive, regional, clockwise P–T path. Peak conditions were followed by decompression and increasing T, leading to retrograde overprinting (Fig. 10A). Mylonitic microtextures, including mica fishes, asymmetric K-feldspar σ-clasts, and S–C structures in the intensively deformed parts of the rock, indicate ductile shear deformation along the retrograde path. Additionally, undeformed, prismatic tourmaline crystals suggest a metasomatic overprint following the development of the S2 foliation.

Garnet–kyanite gneiss

The rock exhibits a polymetamorphic character. The M1 metamorphic event is represented by the assemblage of quartz, K-feldspar, $biotite_1$, phengite, $garnet_1$, and rutile. Staurolite is rare, occurring as inclusions within $garnet_1$ porphyroblasts. The GB thermometers and Bt–Ms barometer estimated the growth conditions for $garnet_1$ at ~7.0–7.5 kbar and ~550–600 °C. The Ti-in-biotite thermometer of Henry et al. (2005) suggested higher T conditions, reflecting a non-equilibrium state. The peak conditions of the M1 paragenesis are estimated at P_{max}~7.5–8.5 kbar and T_{max}~600–650 °C (Fig. 10B). Considering the P–T values, the rock underwent progressive,

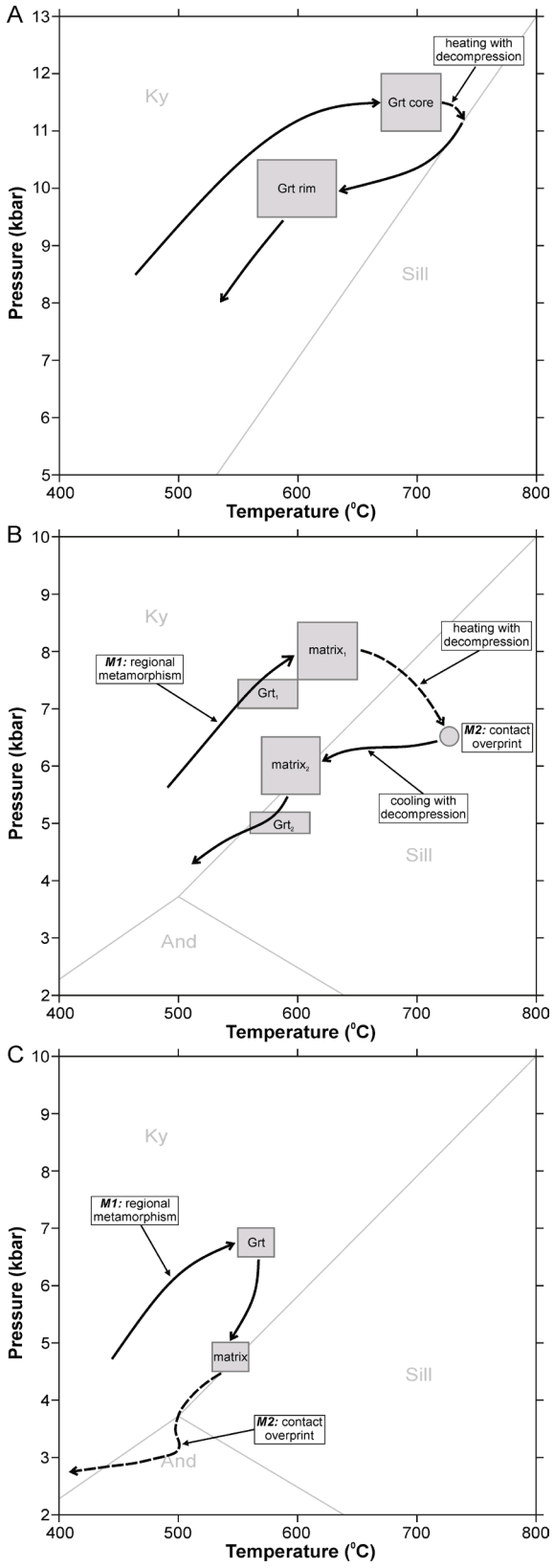

Fig. 10. Proposed metamorphic evolutions of the studied gneisses. Arrows indicate the predicted metamorphic P–T path. **A** — Metamorphic evolution of garnet–biotite gneiss. **B** — Metamorphic evolution of garnet–kyanite gneiss. **C** — Metamorphic evolution of pseudomorph-bearing gneiss.

regional metamorphism, involving chemically homogeneous garnet$_1$ growth and biotite$_1$ formation. The main (S2) and the pre-existing (S1) foliations of the rock resulted from two distinct deformation phases. The garnet$_1$ porphyroblasts are pre-kinematic to the S2.

Fine-grained kyanite aggregates replacing garnet$_1$ porphyroblasts represent the second stage of metamorphism (M2). According to the TWQ modelling of Kondor & M. Tóth (2021), kyanite formed due to the garnet+K-feldspar+H_2O= quartz+kyanite+biotite hydration reaction at T>500 °C and P>4.0 kbar. On the basis of M. Tóth & Vargáné Tóth (2020), the M2 assemblage of the garnet–kyanite gneiss in the adjacent DH area formed at P<6.5 kbar and T of ~730 °C. Although sillimanite should be stable under these conditions, its formation may be hindered by low nucleation rates and the absence of white mica. Since biotite is the dominant mica, this may lead to the formation of metastable kyanite aggregates instead of sillimanite (M. Tóth & Vargáné Tóth 2020). Fine-grained, non-oriented kyanite aggregates suggest intensive nucleation and crystal growth resulting from heating coinciding with decompression. Such conditions are possible in the surroundings of igneous intrusions. Considering this model, the rock was affected by a contact metamorphic (metasomatic) event caused by a granite/granodiorite intrusion following the progressive, regional metamorphic peak (Fig. 10B). Undeformed, idiomorphic tourmaline crystals should also be the result of this metasomatic effect.

The heating was followed by rapid cooling and decompression. Thermobarometric calculations show that mica flakes in the matrix (matrix$_2$) defining the S2 foliation formed under ~5.5–6.5 kbar and ~570–620 °C conditions along the retrograde path. Garnet$_2$ indicates lower P values of ~4.8–5.2 kbar. In contrast, the Ti-in-biotite thermometer (Henry et al. 2005) and the GB thermometer (Ferry & Spear 1978) yielded higher T, while the Ti-in-biotite thermometer by Wu (2020) estimated lower T conditions compared to the matrix$_2$. Given the differences in T values derived from the Ti-in-biotite thermometers, the results are considered uncertain, suggesting non-equilibrium conditions. The GB thermometer suggests that the chemically homogeneous garnet$_2$ idioblasts formed at ~560–610 °C along a continuous retrograde path (Fig. 10B). Sheared, ductilely deformed microtextures (e.g., asymmetric σ-clasts, mica fishes, S–C structures) indicate mylonitic deformation along the retrograde pathway.

Pseudomorph-bearing gneiss

The gneiss shows polymetamorphic features. The M1 mineral assemblage consists of quartz, K-feldspar, biotite, garnet, and rutile. Based on thermobarometric calculations, the peak metamorphic conditions are estimated at P_{max}~6.5–7.0 kbar and T_{max}~550–580 °C for garnet porphyroblasts. The garnet rim and the matrix minerals consistently yielded lower P–T conditions. The thermobarometer of Wu (2020) is associated with significant uncertainty. For biotite and phengite$_1$ (matrix$_1$), this method yielded significantly lower

P–T conditions compared to other methods. Conversely, it provided higher P and T for matrix$_2$ (phengite$_2$) compared to matrix$_1$. The textural position of biotite suggests coexistence with phengite$_1$; therefore, P conditions for phengite$_2$ can only be reliably estimated using the Si-in-phengite barometer. Metamorphic conditions of ~4.5–5.0 kbar and ~540–580 °C could be estimated for matrix minerals, indicating a retrograde metamorphic path following peak conditions (Fig. 10C).

The rock contains kyanite–staurolite aggregates, a few millimetres in size, surrounded by fine-grained white mica (Fig. 4c, d). These aggregates exhibit rhomboidal, cross-shaped, or finger-like forms, resembling andalusite (Fig. 4e). The coexistence of Al_2SiO_5 polymorphs in the same metapelite commonly indicates a non-equilibrium state. Andalusite+sillimanite and kyanite+sillimanite parageneses are the most common, with sillimanite progressively forming from andalusite or kyanite. In contrast, transformations such as sillimanite → andalusite, sillimanite → kyanite, or andalusite → kyanite are generally associated with retrograde, multiphase metamorphic processes (Sánchez-Navas et al. 2012). The andalusite → kyanite reaction can be interpreted in several ways (Whitney 2002; Sepahi et al. 2004; Kim & Ree 2010). Evans & Berti (1986) suggested that an initial contact metamorphic event producing andalusite was overprinted by Barrovian-type metamorphism, resulting in kyanite+staurolite pseudomorphs after andalusite. Similarly, Pitra & Martínez (2024) reported kyanite+staurolite aggregates as retrograde products of an earlier high-T metamorphic event overprinted by lower-grade Barrovian-type metamorphism. According to Martinez et al. (2001), andalusite may form during progressive metamorphism and be overprinted by a retrograde metamorphic event within the stability field of kyanite, producing kyanite aggregates. Sánchez-Navas et al. (2012) noted that although andalusite and kyanite have identical formulae, they cannot be directly transformed into one another. Instead, andalusite initially alters to muscovite, involving mobile components such as K^+ or H_2O, forming a muscovite aureole around the andalusite, while biotite in the surrounding matrix dissolves. Finally, andalusite+biotite and muscovite are replaced by muscovite+kyanite domains. In this reaction, muscovite and biotite act as catalysts, facilitating the andalusite → kyanite transformation and producing a fine-grained muscovite aureole around the kyanite–staurolite pseudomorphs, as observed in the pseudomorph-bearing gneiss.

This reaction, coupled with the morphology and structure of kyanite–staurolite aggregates, suggests the former presence of andalusite. Since andalusite is stable under HT/LP conditions, this implies that following regional metamorphism (M1), the rock may have experienced a contact metamorphic overprint (M2) along a retrograde path, forming andalusite porphyroblasts related to an unidentified magmatic event (Fig. 10C). During retrograde cooling, these porphyroblasts transformed into the kyanite–staurolite aggregates with fine-grained muscovite aureole. Undeformed, idiomorphic tourmaline crystals may also be products of the same contact metasomatic event.

Chlorite schist

The chlorite schist exhibits a well-developed S1 foliation. The chlorite, quartz, K-feldspar, plagioclase feldspar paragenesis represents the M1 assemblage, for which chlorite thermometers estimated a T of ~270–300 °C. Biotite along chlorite bands indicates peak metamorphic conditions near the boundary of the chlorite–biotite zone. The chlorite schist formed under low-grade, greenschist facies progressive regional metamorphism, followed by a metasomatic overprint, which led to the formation of idiomorphic, hypidiomorphic magnetite, as well as copper-bearing opaque phases. The metasomatic overprint was followed by shearing (Kondor & M. Tóth 2021).

Metagranite

Mineral composition and microtextural features such as idiomorphic plagioclase feldspar clasts, polygonal microtextured K-feldspar, and euhedral habit of zircon indicate the igneous origin of this rock type (Vernon & Collins 1988). No mineral assemblages associated with progressive or retrograde metamorphic overprint were identified. The rock displays a slightly developed S1 foliation and an equigranular texture. Sericite bands along S1 planes indicate deformation during the retrograde pathway. Oriented tourmaline grains aligned with the S1 foliation suggest pre-kinematic growth.

Metasomatism

The post-kinematic tourmaline is an essential textural feature in all gneiss varieties, suggesting metasomatic overprinting. In metamorphic rocks, tourmaline, the primary boron (B) reservoir, can form in two ways. Under regional metamorphic conditions, tourmaline may develop within a closed chemical system by utilising the B-content of the protolith (de la Cruz 2021). Organic, clayey sediments provide sufficient B for such processes. The post-kinematic appearance of tourmaline suggests it did not form under regional metamorphic conditions. Since tourmaline is stable across nearly the entire metamorphic P–T field, the availability of B is crucial for its formation. The absence of pre-kinematic tourmaline in the gneisses implies that the B must have derived from an external fluid source, leading to tourmalinisation (Spránitz et al. 2018; Slack 2022). Given the similarities in the optical properties of tourmaline in metagranite and gneisses, it is likely that the granite intrusion in the host gneisses was the source of B. The major limiting factor for post-kinematic tourmaline formation is the amount of B transported by post-magmatic fluids (Trumbull et al. 2020; de la Cruz 2021). The chemical composition of the tourmaline crystals, with an increase in Mg content from core to rim and a decrease in Fe content, suggests a thermally declining hydrothermal system, where the tourmaline grains crystallised from cooling fluids in a distal environment (Fig. 8B).

The gneisses contain idiomorphic ilmenite and rutile needles oriented along foliation planes. In metapelites, the main Ti phase is biotite. During hydrothermal metasomatism, the breakdown of biotite may release Ti, leading to the formation of TiO_2 phases. Given the low solubility of Ti (Ayers & Watson 1993), rutile can nucleate in the textural position of biotite (Rabbia et al. 2009), explaining the orientation of rutile and ilmenite along the foliation planes. The late crystallisation of rutile and ilmenite is thus linked to the metasomatic breakdown of biotite, particularly in biotite-rich zones where more Ti is available (Rabbia et al. 2009). These phases could not crystallise directly from the post-magmatic fluids. Metasomatism, which causes tourmaline crystallisation, is indirectly responsible for the crystallisation of the late TiO_2 phases.

Spatial correlation

The point map of the principal rock types reveals that the primary lithologies are localised within well-defined subregions. Garnet–kyanite gneiss dominates the NW and SE parts of the AH, as well as the northern part of the Ferencszállás dome. Garnet–biotite gneiss is exclusively identified in the Ferencszállás area, while pseudomorph-bearing gneiss occurs in the Kiszombor area. The highest part of the AH is composed of epidote orthogneiss, whereas chlorite schist dominates along a NW–SE-oriented zone (Kondor & M. Tóth 2021). Metagranite is present in boreholes near the northern part of Ferencszállás (Fig. 11). This spatial distribution suggests the presence of a mosaic of blocks with independent metamorphic evolutions in the study area.

To interpret the spatial relationship between these blocks, the metamorphic histories of the principal lithologies must be compared. The evolution of the three main gneiss types can be evaluated within a unified model. All types have S1 and S2 foliation planes, with their first progressive regional metamorphism (M1) characterised by the paragenesis of quartz, K-feldspar, biotite, garnet, rutile, and phengite. Thermobarometric calculations indicate a clockwise metamorphic path for each gneiss, with garnet+biotite assemblages preserving the peak metamorphic conditions. Variations in P_{max} and T_{max} values suggest metamorphism at different crustal depths within the garnet stability field. The primary differences between gneisses are marked by the mineral assemblage associated with the M2 metamorphic overprint. This overprint is linked to a contact metamorphic event in garnet–kyanite gneiss and pseudomorph-bearing gneiss, leading to the formation of fine-grained kyanite aggregates and tourmaline crystals. The difference is the precursor phase of kyanite: in garnet–kyanite gneiss, kyanite aggregates replace garnet, whereas in pseudomorph-bearing gneiss, they are suggested to be pseudomorphs after andalusite. CL observations show colour differences between the two kyanite varieties, indicating variations in chemical composition (Fig. 12). Red CL colour indicates Cr^{3+} substitution, with varying peak intensities reflecting differences in Cr^{3+} concentrations and T (Müller et al. 2016). In garnet–kyanite gneiss, higher peak intensity suggesting higher Cr^{3+} concentrations and T conditions during kyanite formations. Conversely, pseudomorph-bearing gneiss shows lower intensities, indicating lower Cr^{3+} concentration and T (Fig. 12). These differences imply distinct metamorphic conditions or variations in protolith, supporting varied genetic histories for the kyanite-bearing gneisses. Since andalusite is stable at low-P and kyanite at medium- to high-P, the contact metamorphic overprint likely affected the garnet–kyanite gneiss at a deeper crustal level.

The garnet–biotite gneiss is of monometamorphic origin, with no textural evidence of contact metamorphism or the formation of secondary kyanite or andalusite, distinguishing its evolution from that of kyanite-bearing gneisses. Contact metasomatic effects from an igneous intrusion are indicated exclusively by undeformed, post-kinematic tourmaline grains. Although the contact metamorphic (metasomatic) overprint diversely affected the three gneiss types, they can be interpreted within the same genetic model and together define the middle gneiss terrane. Assuming the M2 parageneses are related to the same granitoid intrusion, the gneisses had to be affected by contact metamorphism at

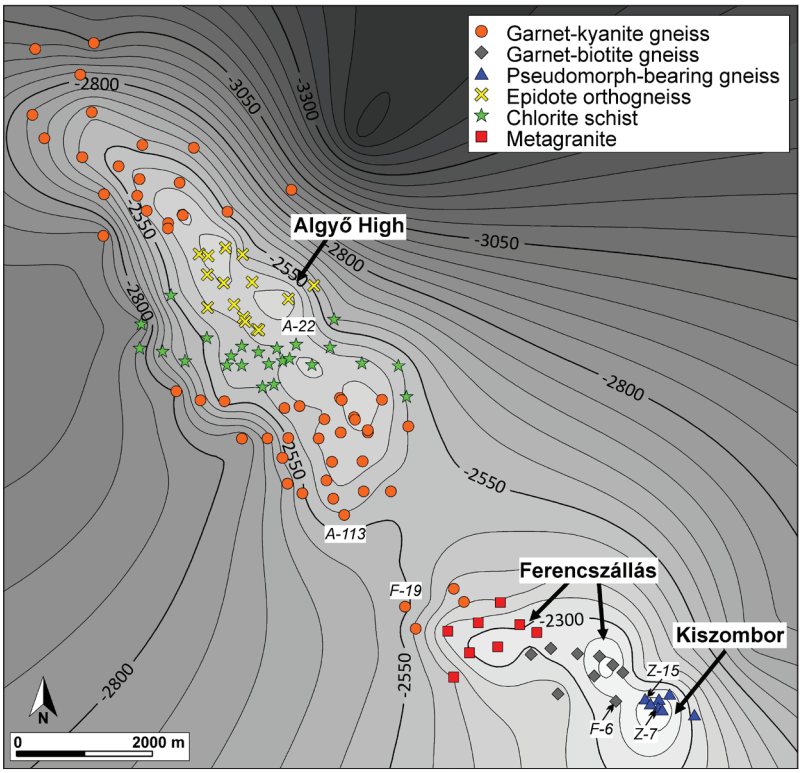

Fig. 11. Contour map of the basement of the AFK area. Symbols on the point map represent the primary lithology of the boreholes.

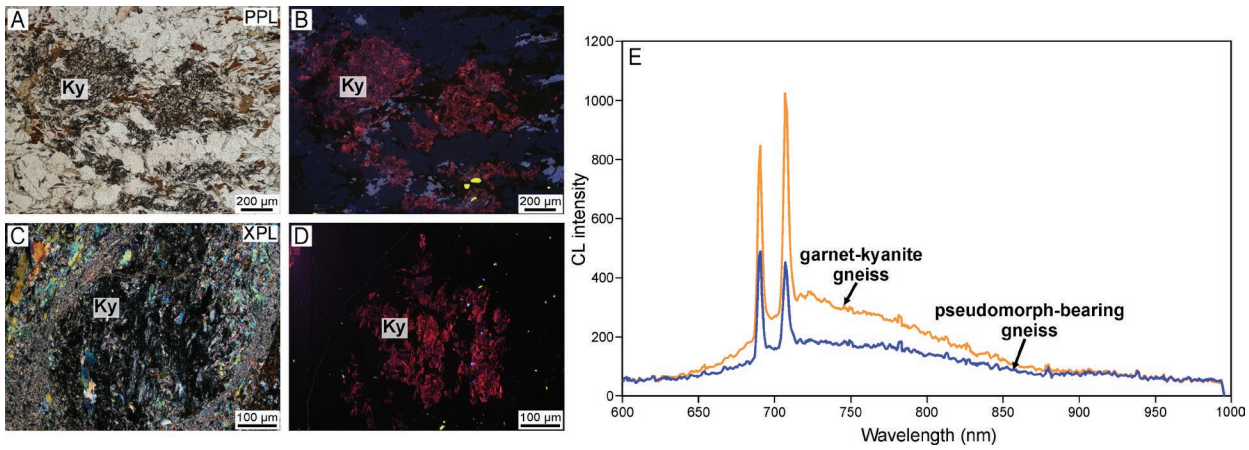

Fig. 12. Cathodoluminescence (CL) observation. **A** — Microphotograph of garnet–kyanite gneiss. **B** — Kyanite aggregates with red CL colour in garnet–kyanite gneiss **C** — Microphotograph of pseudomorph-bearing gneiss. **D** — Kyanite aggregates with red CL colour in pseudomorph-bearing gneiss. **E** — Representative CL spectra of kyanite from different gneisses. PPL: plane-polarised light; XPL: crossed-polarised light.

different crustal depths. The protolith of the metagranite in the Ferencszállás area is likely the intrusive body responsible for the M2 overprint. Currently, the three members of the middle gneiss terrane form a horizontal sequence of blocks without any continuous transition. Consequently, post-metamorphic structural boundaries must separate them.

The metamorphic evolution of epidote orthogneiss and chlorite schist differs significantly from that of the previously described gneisses, suggesting the presence of structural boundaries between the low- and medium-grade units (Kondor & M. Tóth 2021). Kondor & M. Tóth (2021) proposed that these two low-grade rocks represent blocks with different metamorphic evolutions, separated by post-metamorphic structural boundaries (Fig. 13). Considering the spatial positions of the primary lithologies, the metamorphic basement of the AFK area comprises well-defined blocks with diverse metamorphic evolutions. The low-grade units occupy the highest structural position, while the medium-grade gneisses are found at lower structural level.

Geological evolution

The crystalline basement of the AFK area is lithologically heterogeneous, comprising predominantly gneisses, including rocks previously described as mica schists, intercalated with amphibolite lenses (Szalay 1977; Szederkényi 1984; T. Kovács & Kurucz 1984; Kondor & M. Tóth 2021), as well as low-grade rocks occupying the shallowest structural positions (Kondor & M. Tóth 2021). Although previous publications referred to some lithologies as mica schists, detailed petrographic analysis indicates that these rocks represent mica-rich or altered domains of the gneisses. Earlier studies (Szederkényi 1984; Lelkes-Felvári et al. 2005) described the metamorphic basement of the area as a single lithostratigraphic unit, the so-called Dorozsma Complex, and assumed a uniform polymetamorphic evolution for the entire basement. Previous works (Szalay 1977; Szederkényi 1984; T. Kovács & Kurucz 1984; Horváth & Árkai 2002; Lelkes-Felvári et al. 2003, 2005; Kondor & M. Tóth 2021) generally agree that the gneisses experienced an initial progressive, amphibolite facies, regional metamorphism. According to Lelkes-Felvári et al. (2003), the first event was an HT–LP metamorphism, interpreted to be of Permo–Triassic age (273±2 Ma), while Horváth & Árkai (2002) do not rule out its Alpine origin. In both interpretations, this event was followed by an eo-Alpine MP–MT overprint (Horváth & Árkai 2002; Lelkes-Felvári et al. 2003). However, these models did not consider the internal lithological and metamorphic heterogeneity of the basement. Based on comprehensive petrological analyses, the basement of the AFK area comprises distinct lithologies with individual metamorphic histories, that cannot be described by a single, uniform P–T path.

The three genetically related medium-grade gneisses underwent an initial progressive, amphibolite facies, regional metamorphism at different crustal depths. The main difference between the gneisses lies in the physical conditions of the M2 contact metamorphism, presumably related to a granitoid intrusion. Earlier studies demonstrated that during the Late Cretaceous, granite/granodiorite (banatite) intruded the metamorphic terrane, resulting in a metasomatic overprint and tourmaline crystallisation within the host gneisses (Szalay 1977; Szederkényi 1984; Berza et al. 1998). The protolith of the metagranite in the Ferencszállás area is considered the likely source of this contact overprint. Published Late Cretaceous Ar–Ar plateau ages (Lelkes-Felvári et al. 2003; Balogh & Pécskay 2001) are assumed to be associated with this contact metamorphism. Horváth & Árkai (2002) also interpreted the second metamorphic stage as an Alpine event.

Considering the blocks with independent metamorphic histories in the region, including the Algyő–Ferencszállás and the Dorozsma crystalline highs to the west, numerous post-metamorphic structural zones likely separate these units.

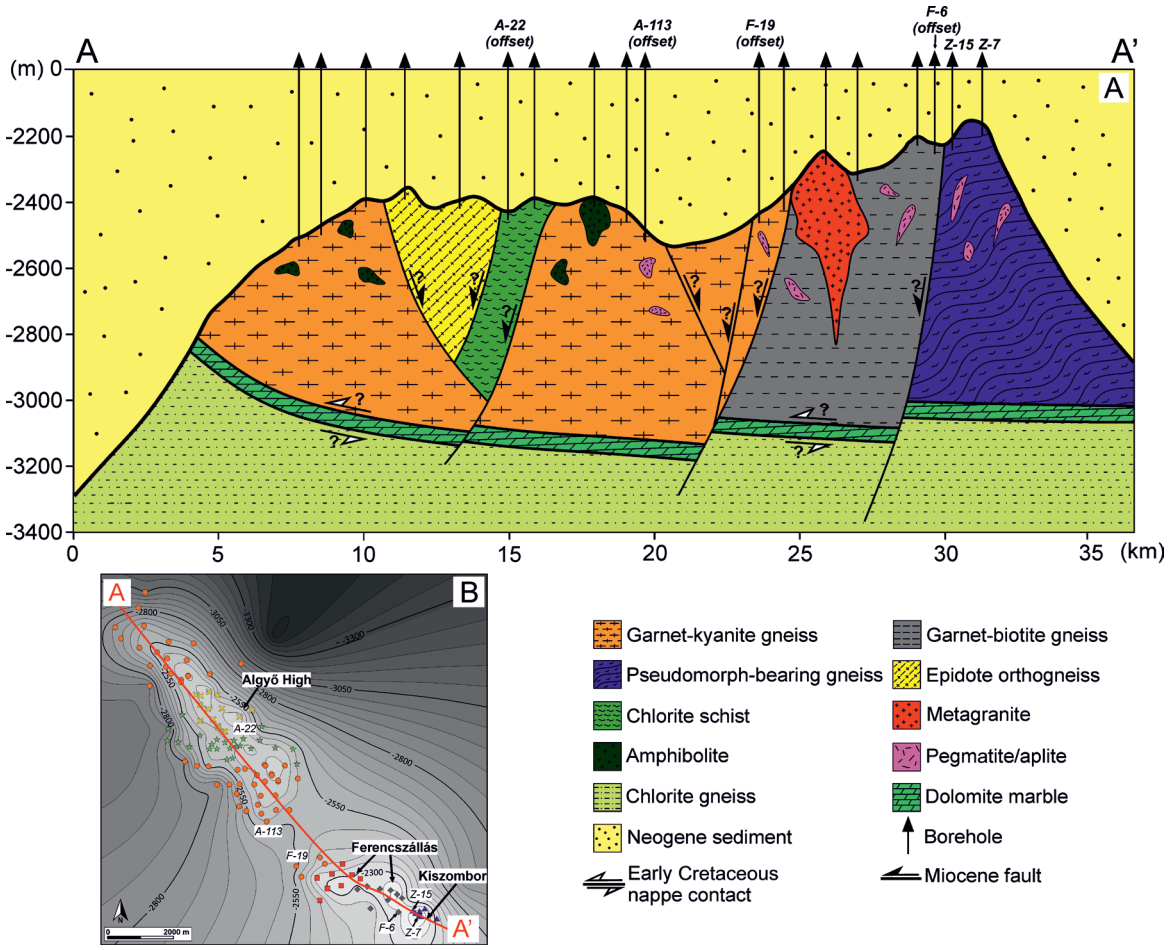

Fig. 13. Schematic geological section of the Algyő–Ferencszállás–Kiszombor area. **A** — Cross-section across the studied area along the A–A' line. **B** — Contour map of the area indicating the line of the cross-section.

The dolomite marble cataclasite zone mapped in the DH is interpreted as a large-scale brittle shear zone within the crystalline basement (M. Tóth 2008; M. Tóth & Vargáné Tóth 2020), associated with Early Cretaceous nappe stacking due to the Alpine orogeny (Reiser et al. 2017a, b). This horizon delineates the boundary between the lowermost medium-grade, amphibolite-dominated block and the overlying higher-grade, garnet–kyanite gneiss domain. Post-kinematic sulphide phases in the dolomite marble suggest that the metasomatic overprint post-dated the deformation (M. Tóth & Vargáné Tóth 2020), indicating that the metasomatic event was caused by a younger, probably Late Cretaceous igneous activity. Based on petrological similarities, Kondor & M. Tóth (2021) propose a similar three-part structure for the AH area, suggesting the eastern continuation of the Alpine thrust sheet beneath the garnet–kyanite gneiss blocks in the AFK area (Fig. 13). In the AFK area, opposite to the Dorozsma case, the middle gneiss terrane can be subdivided into lithological blocks with distinct evolutions. Although the garnet–biotite, garnet–kyanite, and pseudomorph-bearing gneiss varieties are assumed to be separated by post-metamorphic structural zones formed after the Late Cretaceous, no direct information is available on the exact position and age of these boundaries.

The central part of the AH comprises unique low-grade structural blocks that have not been previously documented in the surrounding area. Although post-kinematic mineralisation is also characteristic of the chlorite schist, the metasomatic phases in these rocks differ significantly from those in the gneisses (sulphide minerals vs. tourmaline). If both parageneses are the result of the banatite magmatism, the medium- and low-grade blocks must have been located at significantly different crustal depths during the metasomatic overprint. This suggests that the blocks were juxtaposed after the Late Cretaceous (Kondor & M. Tóth 2021). Furthermore, if the contact metasomatism occurred during the Late Cretaceous, the current structural contact between the blocks must have resulted from an even younger tectonic event.

Sin-rift extension during the middle Miocene led to the formation of metamorphic core complexes along normal fault systems within the crystalline basement of the Pannonian Basin (Tari et al. 1992; Tari 1996). Geophysical studies (Rumpler & Horváth 1988; Posgay et al. 1996; Tari et al. 1999; Matenco & Radivojevic 2012) show that the metamorphic

basement of the AFK area is part of a WSW–ENE-oriented core complex system. As the largest-scale Cenozoic structural event, the low-grade blocks in the central part of the AFK were probably moved to their current position due to the subsidence of the Pannonian Basin during the Miocene extension. In our model, this tectonic event is also responsible for segmenting the middle gneiss realm (Fig. 13).

The extensional event was followed by a post-rift thermal sag phase, causing the subsidence of the Pannonian Basin and the deposition of Neogene sediments across the entire region (Horváth & Tari 1999). Basement highs play a crucial role in hydrocarbon migration, facilitating the accumulation of hydrocarbons in the sedimentary rocks across the Pannonian Basin (Schubert et al. 2007; M. Tóth 2008; Nagy et al. 2013; Molnár et al. 2015; M. Tóth & Vargáné Tóth 2020). The Neogene sedimentary rocks surrounding the AFK metamorphic basement also serve as significant productive hydrocarbon reservoirs, with the basement forming an essential part of this local HC system. The presumed post-metamorphic structural boundaries between blocks with different metamorphic histories could either provide migration pathways from adjacent basins (Szeged Basin and Makó Trough) or act as reservoirs.

Conclusion

The crystalline basement of the Algyő–Ferencszállás–Kiszombor (AFK) area comprises distinct lithological blocks with different metamorphic evolutions. Petrographic and mineral chemistry analyses, combined with thermobarometric calculations, revealed three main types of gneiss that underwent regional amphibolite facies metamorphism (M1), followed by a contact metamorphic (metasomatic) overprint (M2). The M1 event is interpreted as related to the Variscan orogeny, whereas the M2 overprint likely resulted from an Alpine magmatic event. The presence of undeformed tourmaline further supports a metasomatic event associated with granite intrusion, most likely represented by the metagranite body in the Ferencszállás area. The spatial separation of the different gneiss types, along with the occurrence of chlorite schist and epidote orthogneiss in structurally shallower positions, indicates that the AFK basement consists of a mosaic of blocks with distinct metamorphic histories. These blocks are presumably separated by post-metamorphic structural boundaries, which are thought to have developed during Miocene extensional processes following Cretaceous nappe formation.

This study confirms that the AFK crystalline basement is not a single lithostratigraphic unit, but rather a structurally complex metamorphic formation. Brittle structural boundaries between blocks may serve as migration pathways for hydrocarbon or act as fluid reservoirs, analogous to other buried hill systems in the Pannonian Basin. The results provide a new geological model for the metamorphic evolution of the region and emphasise the importance of detailed basement characterisation in hydrocarbon exploration.

Acknowledgement: The MOL Hungarian Oil and Gas Company is thanked for providing thin sections and core samples for investigation. We are grateful to the Faculty of Science Research and Instrument Core Facility of Eötvös Loránd University for allowing mineral composition measurement. We thank Thomas Lange for his assistance during the measurements. The research was financially supported by the National Research, Development and Innovation Office (Grant No. K-138919).

References

Ayers J.C. & Watson E.B. 1993: Rutile solubility and mobility in supercritical aqueous fluids. *Contributions to Mineralogy and Petrology* 114, 321–330. https://doi.org/10.1007/BF01046535

Babinszki E. & Kovács Zs. 2018: Hydrocarbon exploration areas in Hungary – Szeged Basin and the Kiskunság. In: Kovács Zs. (Ed.): Hydrocarbons in Hungary. *Hungarian Energy and Public Utility Regulatory Authority*, Budapest, 83–105.

Balogh K. & Pécskay Z. 2001: K/Ar and Ar/Ar geochronological studies in the PANCARDI region. *Acta Geologica Hungarica* 44, 281–299.

Berza T., Constantinescu E. & Vlad S. 1998: Upper Cretaceous magmatic series and associated mineralization in the Carpathian–Balkan orogen. *Resource Geology* 48, 291–306. https://doi.org/10.1111/j.1751-3928.1998.tb00026.x

Caddick T. & Thompson A.B. 2008: Quantifying the tectono-metamorphic evolution of pelitic rocks from a wide range of tectonic settings: Mineral compositions in equilibrium. *Contributions to Mineralogy and Petrology* 156, 177–195. https://doi.org/10.1007/s00410-008-0280-6

Cathelineau M. 1988: Cation site occupancy in chlorites and illites as a function of temperature. *Clay Minerals* 23, 471–485. https://doi.org/10.1180/claymin.1988.023.4.13

Cathelineau M. & Nieva D. 1985: A chlorite solid solution geothermometer the Los Azufres (Mexico) geothermal system. *Contributions to Mineralogy and Petrology* 91, 235–244. https://doi.org/10.1007/BF00413350

Csontos L., Nagymarosy A., Horváth F. & Kováč M. 1992: Cenozoic evolution of the Intra-Carpathian area: A model. *Tectonophysics* 208, 221–241. https://doi.org/10.1016/0040-1951(92)90346-8

Csontos L. & Vörös A. 2004: Mesozoic plate tectonic reconstruction of the Carpathian region. *Palaeogeography, Palaeoclimatology, Palaeoecology* 210, 1–56. https://doi.org/10.1016/j.palaeo.2004.02.033

De la Cruz E. 2021: Tourmaline of the Kragerø pegmatites. The source of boron and its implication for the melt formation of Sveconorwegian pegmatites. *Master thesis, University of Oslo.*

Deer W.A., Howie R.A. & Zussman J. 1963: Rock forming minerals. Vol. 2: Chain silicates. *Longmans*, London.

Evans B.W. & Berti J.W. 1986: A revised metamorphic history for the Chiwaukum schist, North Cascades, Washington. *Geology* 14, 695–698. https://doi.org/10.1130/0091-7613(1986)14<643:EMFMSI>2.0.CO;2

Ferry J.M. & Spear F.S. 1978: Experimental calibration of the partitioning of Fe and Mg between biotite and garnet. *Contributions to Mineralogy and Petrology* 66, 113–117. https://doi.org/10.1007/BF00372150

Fodor L., Csontos L., Bada G., Győrfi I. & Benkovics L. 1999: Tertiary tectonic evolution of the Pannonian Basin system and neighbouring orogens: a new synthesis of paleostress data. The Mediterranean basins: Tertiary extension within the Alpine orogene. *Geological Society, London, Special Publication* 156, 295–334. https://doi.org/10.1144/GSL.SP.1999.156.01.25

Forbes W.C. & Flower M.F.J. 1974: Phase relations of titan-phlogopite, $K_2Mg_4TiAl_2Si_6O_{20}(OH)_4$: a refractory phase in the upper mantle? *Earth and Planetary Science Letters* 22, 60–66. https://doi.org/10.1016/0012-821X(74)90064-8

Haas J. 2001: Geology of Hungary. *Eötvös University Press*, Budapest.

Haas J., Budai T., Csontos L., Fodor L. & Konrád Gy. 2010: Pre-Cenozoic Geological Map of Hungary 1:500 000. *Geological Institute of Hungary*. https://map.mbfsz.gov.hu/preterc500/

Henry D.J. & Guidotti C.V. 2002: Titanium in biotite from metapelitic rocks: Temperature effects, crystal-chemical controls, and petrologic applications. *American Mineralogist* 87, 375–382. https://doi.org/10.2138/am-2002-0401

Henry D.J., Guidotti C.V. & Thomson J.A. 2005: The Ti-saturation surface for low-to-medium pressure metapelitic biotite: Implications for geothermometry and Ti-substitution mechanisms. *American Mineralogist* 90, 316–328. https://doi.org/10.2138/am.2005.1498

Hillier S. & Velde B. 1991: Octahedral occupancy and the chemical composition of diagenetic (Low-Temperature) Chlorites. *Clay Minerals* 26, 149–168. https://doi.org/10.1180/claymin.1991.026.2.01

Holdaway M.J. 2000: Application of new experimental and garnet Margules data to the garnet–biotite geothermometer. *American Mineralogist* 85, 881–892. https://doi.org/10.2138/am-2000-0701

Horváth F. & Tari G. 1999: IBS Pannonian Basin project: a review of the main results and their bearings on hydrocarbon exploration. The Mediterranean basins: Tertiary extension within the Alpine orogene: *Geological Society, London, Special Publication* 156, 195–213. https://doi.org/10.1144/gsl.sp.1999.156.01.11

Horváth P. & Árkai P. 2002: Pressure-temperature path of metapelites from the Algyő–Ferencszállás area, SE Hungary: thermobarometric constraints from coexisting mineral assemblages and garnet zoning. *Acta Geologica Hungarica* 45, 1–27. https://doi.org/10.1556/ageol.45.2002.1.1

Jowett E.C. 1991: Fitting iron and magnesium into the hydrothermal chlorite geothermometer. In: *GAC/MAC/SEG Joint Annual Meeting, Program with Abstracts* ,Toronto, 16, A62.

Kamzolkin V.A., Ivanov S.D. & Konilov A.N. 2016: Empirical Phengite Geobarometer: background, calibration, and application. *Geology of Ore Deposits* 58, 613–622. https://doi.org/10.1134/S1075701516080092

Kim H.S. & Ree J.H. 2010: P-T modelling of kyanite and sillimanite paramorphs growth after andalusite in late Paleozoic Pyeongan Supergroup, South Korea: Implication for metamorphism during the Mesozoic tectonic evolution. *Lithos* 118, 269–286. https://doi.org/10.1016/j.lithos.2010.05.005

Kondor H. & M. Tóth T. 2021: Contrasting metamorphic and post-metamorphic evolutions within the Algyő basement high (Tisza Mega-unit, SE Hungary). Consequences on structural history. *Central European Geology* 64, 91–112. https://doi.org/10.1556/24.2021.00004

Kranidiotis P. & MacLean W.H. 1987: Systematics of chlorite Alteration at the Phelps Dodge Massive Sulfide deposit, Matagami, Quebec. *Economic Geology* 82, 1898–1911. https://doi.org/10.2113/gsecongeo.82.7.1898

Lelkes-Felvári Gy., Frank W. & Schuster R. 2003: Geochronological constraints of the Variscan, Permian-Triassic and eo-Alpine (Cretaceous) evolution of the Great Hungarian Plain basement. *Geologica Carpathica* 54, 267–280.

Lelkes-Felvári Gy., Schuster R., Frank W. & Sassi R. 2005: Metamorphic history of the Algyő High (Tisza Mega-unit, basement of Great Hungarian Plain) - a counterpart of crystalline units of the Koralpe-Wölz nappe system (Austroalpine, Eastern Alps). *Acta Geologica Hungarica* 48, 371–394. https://doi.org/10.1556/ageol.48.2005.4.2

M. Tóth T. 2008: Repedezett, metamorf fluidumtárolók az Alföld aljzatában. *D.Sc. Thesis* (in Hungarian)

M. Tóth T. & Vargáné Tóth I. 2020: Lithologically controlled behaviour of the Dorozsma metamorphic hydrocarbon reservoir (Pannonian Basin, SE Hungary). *Journal of Petroleum Science and Engineering* 195. https://doi.org/10.1016/j.petrol.2020.107748

M. Tóth T., Vass I., Szanyi J. & Kovács B. 2007: Water and heat flow through uplifted metamorphic highs in the basement of the Pannonian Basin. In: XXXV. IAH Congress, Lisbon, Groundwater and Ecosystems, Proceedings, 1–10.

M. Tóth T., Fiser-Nagy Á., Kondor H., Molnár L., Schubert F., Vargáné Tóth I. & Zachar J. 2021: Az Alföld metamorf aljzata: a köztes tömegtől a tarka mozaikig. *Földtani Közlöny* 151, 3–26. https://doi.org/10.23928/foldt.kozl.2021.151.1.3

Martinez F.J., Reche J. & Arboleya M.L. 2001: P-T modelling of the andalusite-kyanite-andalusite sequence and related assemblages in high-Al graphitic pelites: prograde and retrograde paths in a late kyanite belt in the Variscan Iberia. *Journal of Metamorphic Geology* 19, 661–677. https://doi.org/10.1046/j.0263-4929.2001.00335.x

Massonne H.J. & Schreyer W. 1987: Phengite geobarometry based on the limiting assemblage with K-feldspar, phlogopite, and quartz. *Contributions to Mineralogy and Petrology* 96, 212–224. https://doi.org/10.1007/BF00375235

Matenco L. & Radivojević D. 2012: On the formation and evolution of the Pannonian Basin: Constraints derived from the structure of the junction area between the Carpathians and Dinarides. *Tectonics* 31. https://doi.org/10.1029/2012TC003206

Molnár L., M. Tóth T. & Schubert F. 2015: Structural controls on the petroleum migration and entrapment within faulted basement blocks of the Szeghalom Dome (Pannonian Basin, SE Hungary). *Geologia Croatica*, 68, 247–259. https://doi.org/10.4154/GC.2015.19

Müller A., van den Kerkhof A.M., Selbekk R.S. & Broekmans M.A.T.M. 2016: Trace element composition and cathodoluminescence of kyanite and its petrogenetic implications. *Contributions to Mineralogy and Petrology* 171, 70. https://doi.org/10.1007/s00410-016-1280-6

Nagy Á., M. Tóth T., Vásárhelyi B. & Földes T. 2013: Integrated core study of a fractured metamorphic HC-reservoir; Kiskunhalas-NE, Pannonian Basin. *Acta Geodaetica et Geophysica* 48, 53–75. https://doi.org/10.1007/s40328-012-0008-y

Neubauer F. 2002: Contrasting Late Cretaceous to Neogene ore provinces in the Alpine–Balkan–Carpathian–Dinaride collision belt. The Timing and Location of Major Ore Deposits in an Evolving Orogen. *Geological Society, London, Special Publications* 204, 81–202. https://doi.org/10.1144/GSL.SP.2002.204.01.06

Pirajno F. & Smithies R.H. 1992: The FeO/(FeO+MgO) ratio of tourmaline: A useful indicator of spatial variations in granite-related hydrothermal mineral deposits. *Journal of Geochemical Exploration* 42, 71–31. https://doi.org/10.1016/0375-6742(92)90033-5

Pitra P. & Martínez F.J. 2024: Incomplete Hydration during 'Retrograde' Metamorphism: 'Barrovian' Kyanite-, Staurolite-, Chloritoid-Bearing Pseudomorphs after Andalusite (Cap de Creus, E Pyrenees, Spain). *Journal of Petrology* 65. https://doi.org/10.1093/petrology/egae004

Posgay K., Takács E., Szalai I., Bodoky T., Hegedűs E., Jánváriné K.I., Tímár Z., Varga G., Bérczi I. & Szalay Á. 1996: International deep reflection survey along the Hungarian Geotraverse. *Geophysical Transactions* 40, 1–44.

Rabbia O.M., Hernández L.B., French D.H. & King R.W. 2009: The El Teniente porphyry Cu–Mo deposit from a hydrothermal rutile perspective. *Mineralium Deposita* 44, 849–866. https://doi.org/10.1007/s00126-009-0252-4

Reiser M.K. 2015: The tectonometamorphic evolution of the Apuseni Mountains during the Cretaceous, Investigation on the interplay between tectonics and surface processes in the build-up of a source area. *Dissertation*, University of Innsbruck.

Reiser M.K., Schuster R., Spikings R., Tropper P. & Fügenschuh B. 2017a: From nappe stacking to exhumation: Cretaceous tectonics in the Apuseni Mountains (Romania). *International Journal of Earth Sciences* 106, 659–685. https://doi.org/10.1007/s00531-016-1335y

Reiser M.K., Schuster R., Spikings R., Tropper P. & Fügenschuh B. 2017b: Constraints on the depositional and tectonometamorphic evolution of marbles from the Biharia Nappe System (Apuseni Mountains, Romania). *Geologica Carpathica* 68, 147–164. https://doi.org/10.1515/geoca-2017-0012

Robert J.L. 1976: Titanium solubility in synthetic phlogopite solid solutions. *Chemical Geology* 17, 213–227. https://doi.org/10.1016/0009-2541(76)90036-X

Rumpler J. & Horváth F. 1988: Some representative seismic reflection lines from the Pannonian basin and their structural interpretation. The Pannonian basin – A study in basin evolution. *AAPG Memoir* 45, 53–169. https://doi.org/10.1306/M45474C13

Sánchez-Navas A., De Oliveira-Barbosa R., García-Casco A. & Martín-Algarra A. 2012: Transformation of andalusite to kyanite in the Alpujarride Complex (Betic Cordillera, Southern Spain): Geologic Implications. *The Journal of Geology* 120, 557–574. https://doi.org/10.1086/666944

Schmid S.M., Bernoulli D., Fügenschuh B., Matenco L., Schefer S., Schuster R., Tischler M. & Ustaszewski K. 2008: The Alpine-Carpathian-Dinaridic orogenic system: correlation and evolution of tectonic units. *Swiss Journal of Geosciences* 101, 139–183. https://doi.org/10.1007/s00015-008-1247-3

Schmid S.M., Fügenschuh B., Kounov A., Mațenco L., Nievergelt P., Oberhänsli R., Pleuger J., Schefer S., Schuster R., Tomljenović B., Ustaszewski K. & van Hinsbergen D.J.J. 2020: Tectonic units of the Alpine collision zone between Eastern Alps and western Turkey. *Gondwana Research* 78, 308–374. https://doi.org/10.1016/j.gr.2019.07.005

Schubert F., Diamond L.W. & M. Tóth T. 2007: Fluid-inclusion evidence of petroleum migration through a buried metamorphic dome in the Pannonian Basin, Hungary. *Chemical Geology* 244, 357–381. https://doi.org/10.1016/j.chemgeo.2007.05.019

Sepahi A.A., Whitney D.L. & Baharifar A.A. 2004: Petrogenesis of andalusite-kyanite-sillimanite veins and host rocks, Sanandaj–Sirjan metamorphic belt, Hamadan, Iran. *Journal of Metamorphic Geology* 22, 119–134. https://doi.org/10.1111/j.1525-1314.2004.00502.x

Slack J.F. 2022: Perspectives on premetamorphic stratabound tourmalinites. *Journal of Geosciences* 67, 73–102. http://doi.org/10.3190/jgeosci.349

Spránitz T., Józsa S., Váczi B. & Török K. 2018: Magmatic and metamorphic evolution of tourmaline-rich rocks of the Sopron area, Eastern Alps (W-Hungary). *Journal of Geosciences* 63, 175–191. http://doi.org/10.3190/jgeosci.263

Szalay Á. 1977: Metamorphic-granitogenic rocks of the basement complex of the Great Hungarian Plain, Eastern Hungary. *Acta Mineralogica-Petrographica* 23, 49–69.

Szederkényi T. 1984: Az Alföld kristályos aljzata és földtani kapcsolatai. *D.Sc. Thesis* (in Hungarian).

Szederkényi T. 2007: Banatite association in the basement of the southern part of the Great Hungarian Plain. *Acta GGM Debrecina Geology, Geomorphology, Physical Geography Series* 2, 67–77.

T. Kovács G. & Kurucz B. 1984: A Dél-Alföld mezozoikumnál idősebb képződményei. *Magyar Állami Földtani Intézet alkalmi kiadványa*, Budapest, 15–19.

Tari G. 1996: Extreme crustal extension in the Rába River extensional corridor (Austria/Hungary). *Mitteilungen der Gesellschaft der Geologie-und Bergbaustudenten in Österreich* 41, 1–17.

Tari G., Horváth F. & Rumpler J. 1992: Styles of extension in the Pannonian Basin. *Tectonophysics* 208, 203–219. https://doi.org/10.1016/0040-1951(92)90345-7

Tari G., Dövényi P., Dunkl I., Horváth F., Lenkey L., Stefanescu M., Szafián P. & Tóth T. 1999: Lithospheric structure of the Pannonian Basin derived from seismic, gravity and geothermal data. The Mediterranean basins: Tertiary extension within the Alpine orogene: *Geological Society, London, Special Publications* 156, 215–250. https://doi.org/10.1144/GSL.SP.1999.156.01.12

Trumbull R.B., Codeco M.S., Jiang S.Y., Palmer M. & Slack J.F. 2020: Boron isotope variations in tourmaline from hydrothermal ore deposits: A review of controlling factors and insights for mineralizing systems. *Ore Geology Reviews* 125. https://doi.org/10.1016/j.oregeorev.2020.103682

Vass I., M. Tóth T., Szanyi J. & Kovács B. 2009: Water and heat flow through uplifted metamorphic highs in the basement of the Pannonian Basin. In: M. Tóth T. (Eds): Igneous and metamorphic rocks of the Tisza Unit. *Geolitera Press*, Szeged, 325–339 (in Hungarian with English abstract).

Vernon R.H. & Collins W.J. 1988: Igneous microstructures in migmatites. *Geology* 16, 1126–1129. https://doi.org/10.1130/0091-7613(1988)016<1126:IMIM>2.3.CO;2

Whitney D.L. 2002: Coexisting andalusite, kyanite, and sillimanite: sequential formation of three Al_2SiO_5 polymorphs during progressive metamorphism near the triple point, Sivrihisar, Turkey. *American Mineralogist* 87, 405–426. https://doi.org/10.2138/am-2002 0404

Whitney D.L. & Evans B.W. 2010: Abbreviations for names of rock-forming minerals. *American Mineralogist* 95, 185–187. https://doi.org/10.2138/am.2010.3371

Wu C.M. 2019: Original Calibration of a garnet geobarometer in metapelite. *Minerals* 9, 540. https://doi.org/10.3390/min9090540

Wu C.M. 2020: Calibration of the biotite-muscovite geobarometer for metapelitic assemblages devoid of garnet or plagioclase. *Lithos* 372–373, 105668. https://doi.org/10.1016/j.lithos.2020.105668

Wu C.M. & Chen H.X. 2015: Revised Ti-in-biotite geothermometer for ilmenite- or rutile-bearing crustal metapelites. *Earth Science* 60, 116–121. https://doi.org/10.1007/s11434-014-0674-y

Xie X., Byerly G.R. & Ferrell R.E. 1996: IIb trioctahedral chlorite from the Barberton greenstone belt: crystal structure and rock composition constraints with implications to geothermometry. *Contributions to Mineralogy and Petrology* 126, 275–291. https://doi.org/10.1007/s004100050250

Zang W. & Fyfe W.S. 1995: Chloritization of the hydrothermally altered bedrock at the Igarapé Bahia gold deposit, Carajás, Brazil. *Mineralium Deposita* 30, 30–38. https://doi.org/10.1007/BF00208874

Electronic supplementary material is available online:
Supplementary Tables S1, S2 at https://geologicacarpathica.com/data/files/supplements/GC-76-Kondor_TablesS1-S2.docx